The Astrophysical Journal, 723:1447–1468, 2010 November 10 doi:10.1088/0004-637X/723/2/1447

THE FIELD X-RAY AGN FRACTION TO $z = 0.7$ FROM THE *CHANDRA* MULTIWAVELENGTH PROJECT AND THE SLOAN DIGITAL SKY SURVEY

Daryl Haggard[1,2,6], Paul J. Green[3], Scott F. Anderson[1], Anca Constantin[4], Tom L. Aldcroft[3], Dong-Woo Kim[3], and Wayne A. Barkhouse[5]

[1] Department of Astronomy, University of Washington, Box 351580, Seattle, WA 98195, USA; dhaggard@astro.washington.edu
[2] Kavli Institute for Theoretical Physics, University of California, Santa Barbara, CA 93106, USA
[3] Harvard-Smithsonian Center for Astrophysics, 60 Garden Street, Cambridge, MA 02138, USA
[4] Department of Physics and Astronomy, James Madison University, Harrisonburg, VA 22807, USA
[5] Department of Physics and Astrophysics, University of North Dakota, Grand Forks, ND 58202, USA
Received 2010 March 30; accepted 2010 August 31; published 2010 October 22

ABSTRACT

We employ the *Chandra* Multiwavelength Project (ChaMP) and the Sloan Digital Sky Survey (SDSS) to study the fraction of X-ray-active galaxies in the field to $z = 0.7$. We utilize spectroscopic redshifts from SDSS and ChaMP, as well as photometric redshifts from several SDSS catalogs, to compile a Parent sample of more than 100,000 SDSS galaxies and nearly 1600 *Chandra* X-ray detections. Detailed ChaMP volume completeness maps allow us to investigate the local fraction of active galactic nuclei (AGNs), defined as those objects having broadband X-ray luminosities $L_X(0.5\text{–}8\ \mathrm{keV}) \geqslant 10^{42}$ erg s^{-1}, as a function of absolute optical magnitude, X-ray luminosity, redshift, mass, and host color/morphological type. In five independent samples complete in redshift and *i*-band absolute magnitude, we determine the field AGN fraction to be between $0.16\% \pm 0.06\%$ (for $z \leqslant 0.125$ and $-18 > M_i > -20$) and $3.80\% \pm 0.92\%$ (for $z \leqslant 0.7$ and $M_i < -23$). We find excellent agreement between our ChaMP/SDSS field AGN fraction and the *Chandra* cluster AGN fraction, for samples restricted to similar redshift and absolute magnitude ranges: $1.19\% \pm 0.11\%$ of ChaMP/SDSS field galaxies with $0.05 < z < 0.31$ and absolute *R*-band magnitude more luminous than $M_R < -20$ are AGNs. Our results are also broadly consistent with measures of the field AGN fraction in narrow, deep fields, though differences in the optical selection criteria, redshift coverage, and possible cosmic variance between fields introduce larger uncertainties in these comparisons.

Key words: galaxies: active – galaxies: nuclei – surveys – X-rays: galaxies

1. INTRODUCTION

A fundamental constraint on all theories modeling the interplay of supermassive black hole (SMBH) accretion and galaxy evolution should be the fraction of galaxies in the local universe that host actively accreting nuclei. Accretion onto an SMBH is the predominant source of energy produced by active galactic nuclei (AGNs) and QSOs, so a measure of accretion activity (at a variety of redshifts and luminosities) provides a valuable constraint on the black hole mass function at the present day (Soltan 1982; Rees 1984; Marconi et al. 2004).

In both active and inactive galaxies, observations show a remarkably tight correlation between the properties of galactic spheroids and the masses of their central black holes, the M_{BH}–σ relation (Ferrarese & Merritt 2000; Gebhardt et al. 2000; Gültekin et al. 2009), suggesting that SMBHs play an important role in the formation of galactic bulges. Simulations indicate that the black hole and the bulge may co-evolve, each growing as a result of repeated merger events (e.g., Hernquist 1989; Di Matteo et al. 2005; Hopkins et al. 2005, 2008). In this scenario, the merger causes cold gas to fall to the center, triggering starbursts, and fueling rapid black hole growth. Even while accretion inflows increase the black hole's mass, outflows transport energy from the active nucleus to the surrounding host galaxy (e.g., Granato et al. 2004), creating a mechanism by which the galaxy and its central black hole can "feedback" as they evolve. In extreme cases, these outflows can carry enough energy to alter the galaxy's evolution by ejecting gas and truncating star formation.

Several well-studied phenomena support this so-called feedback paradigm, which links star formation and SMBH growth to galaxy mergers. First, the space density of low-luminosity active galactic nuclei (LLAGNs) peaks at lower host mass than that of luminous quasars (Barger et al. 2005; Hasinger et al. 2005; Scannapieco et al. 2005), indicating that AGN may undergo "cosmic downsizing" as do galaxy spheroids (Cowie et al. 1996). Next, the local mass density of SMBHs corresponds closely to the luminosity density produced by quasars at high redshift (Yu & Tremaine 2002; Hopkins et al. 2006). Hence, the present-day population of AGNs and quiescent black holes may represent the fossil record of their brighter, high-redshift counterparts (the QSO luminosity function peaks at redshifts $z \sim 2$), formed at a time when galaxy mergers were common. This suggests that all massive galaxies may have undergone an AGN phase (e.g., Marconi et al. 2004; Shankar et al. 2004).

Though they clearly influence the evolution of galaxies and the conditions in the early universe, fundamental questions about the formation and evolution of accreting black holes remain. To be robust, the merger and feedback paradigm must reproduce the fraction of galaxies hosting AGN, the ratio of obscured to unobscured AGN necessary to match the cosmic X-ray background, the space density of SMBHs, and AGN clustering.

X-ray emission is the most reliable primary signature of AGN activity because X-rays offer the most complete and efficient marker of active accretion close to the black hole (10–100 gravitational radii). Combined with other wavelengths, X-ray observations sample a wide variety of AGNs and improve our census of AGN demographics (Brandt & Hasinger 2005, and references therein).

[6] NASA Harriett G. Jenkins Fellow.

Galaxies that do not harbor a powerful accreting black hole may also produce X-rays due to hot interstellar gas, supernova remnants, and low- and high-mass X-ray binary populations (Fabbiano 2006; Kim et al. 2006); and even in "normal" galaxies an LLAGN may persist (see Ho 2008, for a review). In this work, we consider the X-ray-active fraction of galaxies out to $z = 0.7$, in a field covering more than 20 deg^2, at a wide range of broadband X-ray luminosities ($10^{40} \lesssim L_X$[0.5–8 keV; erg s^{-1}] $\lesssim 10^{46}$), including those characteristic of normal and star-forming galaxies. Since the many X-ray-producing mechanisms described above can muddy the waters in lower-X-ray luminosity systems, we focus the bulk of our analysis on sources with X-ray luminosities $L_X(0.5\text{–}8\ \mathrm{keV}) \geqslant 10^{42}$ erg s^{-1}, characteristic of accreting SMBHs.

Measurements of the AGN fraction as a function of environment have been made using both optical spectroscopic samples and optical/radio-selected samples. Kauffmann et al. (2004) use emission-line galaxies in the Sloan Digital Sky Survey (SDSS; York et al. 2000) to measure the fraction as a function of environment and find that the fraction of very luminous AGN decreases with increasing environmental density (see also Popesso & Biviano 2006); while less luminous SDSS AGNs show no such trend (Miller et al. 2003; Kauffmann et al. 2004). Studies of the radio-loud SDSS AGN fraction demonstrate that the fraction of galaxies hosting radio-loud AGN increases toward richer environments (except at the highest emission-line luminosities; Best et al. 2005).

As in field studies, X-ray identification of AGN activity in clusters has proved to be even more efficient than optical or radio techniques, particularly for low-luminosity AGNs. A significant body of work on the cluster AGN fraction has been enabled by a combination of *Chandra* X-ray observations and spectroscopic follow-up for a series of 32 clusters with $0.05 < z < 1.3$ (Martini et al. 2002, 2006, 2007, 2009). These authors find larger AGN fractions in clusters than those found in optical emission-line studies. One of the aims of the present work is to make a detailed comparison between the field and cluster X-ray AGN fractions based on a combination of *Chandra* imaging and ground-based optical photometry.

NASA's *Chandra X-ray Observatory* (Weisskopf et al. 2002) has generated a rich archive of X-ray sources, detected with unprecedented resolution and sensitivity. By cross-correlating the *Chandra* archive with the SDSS—an extensive optical survey in five filters—it is possible to identify X-ray counterparts to individual optical objects, confirming their classification as quasars or AGNs. The *Chandra* Multiwavelength Project (ChaMP; Green et al. 2004, 2009) has carefully analyzed 323 *Chandra* fields (about 30 deg^2) that overlap the SDSS and characterized all optical/X-ray matches. We employ these X-ray and optical surveys to determine the fraction of actively accreting SMBHs (or AGNs) out to redshift of $\sim$0.7. We also explore the AGN fraction as a function of galaxy luminosity, redshift, mass, and host galaxy morphology. Such measures of the AGN fraction will prove useful for constraining the fueling, lifetimes, and growth of central SMBHs.

In Section 2, we describe the Extended ChaMP (*Chandra* Cycles 1–6) and SDSS surveys; in Section 3, we detail the ChaMP/SDSS sample developed for this study, including specifics on the spectroscopic and photometric redshift catalogs we employ. Section 4 outlines our methods for determining *k*-corrections, absolute magnitudes, masses, X-ray and optical luminosities, and our definition of five independent samples complete in redshift and *i*-band absolute magnitude. In Section 5, we describe our determination of the X-ray-active and AGN fractions in these volume-limited optical samples, investigate possible evolution of the fraction with redshift, and trends with absolute magnitude and mass, in addition to providing an assessment of how photometric redshift errors and other selection effects might impact our measure of the AGN fraction. We discuss the AGN fraction as a function of galaxy color and compare our results to others in the field, groups, and clusters in Section 6, and wrap up with our conclusions in Section 7.

We adopt an $H_0 = 70$ km s^{-1} Mpc^{-1}, $\Omega_\Lambda = 0.7$, and $\Omega_M = 0.3$ cosmology throughout.

2. THE X-RAY AND OPTICAL CATALOGS

2.1. The Extended Chandra Multiwavelength Project

ChaMP is a wide-area serendipitous X-ray survey based on archival X-ray images of the $|b| > 20$ deg sky observed with the AXAF CCD Spectrometer (ACIS; Weisskopf et al. 2002) on-board *Chandra*.[7] The full 130-field Cycle 1–2 X-ray catalog is public (Kim et al. 2007b), and the most comprehensive X-ray number counts (log N–log S) to date have been produced thanks to 6600 sources and massive source-retrieval simulations (Kim et al. 2007a).

We have recently expanded our X-ray analysis to cover a total of 392 fields through *Chandra* Cycle 6 (see detailed descriptions in Covey et al. 2008; Green et al. 2009), to improve statistics and encompass a wider range of source types—we refer to this expansion as the Extended ChaMP. The new list of *Chandra* pointings avoids overlapping X-ray observations by eliminating the observation with the shorter exposure time. As described in Green et al. (2004), we also avoid *Chandra* fields with large ($\gtrsim$3′) extended sources in either optical or X-rays (e.g., nearby galaxies M101, NGC 4725, NGC 4457, or clusters of galaxies MKW8, or Abell 1240). Spurious X-ray sources (due to, e.g., hot pixels, bad bias, bright source readout streaks) have been flagged and removed as described in Kim et al. (2007b). For the expansion, we select only *Chandra* fields that overlap SDSS Data Release 5 (DR5) imaging; of the 392 ChaMP fields (observation IDs; hereafter "obsids"), 323 fall within the SDSS DR5 footprint.[8] The Extended ChaMP covers $\sim$30 deg^2 at the brightest fluxes[9] (Green et al. 2009). In addition to SDSS imaging, we have undertaken deep ($r \sim 25$) NOAO/MOSAIC optical imagining (described in Green et al. 2004), work currently being extended to 67 fields (W.A. Barkhouse et al. 2010, in preparation).

We have incorporated spectroscopic information, redshifts, and line diagnostics, for the entire optical catalog from: (1) existing ChaMP spectroscopy (Green et al. 2004), (2) the SDSS Data Release 7 (DR7) spectroscopic catalog (Abazajian et al. 2009), (3) the SDSS DR7 Max Planck Institute for Astrophysics/John's Hopkins University (MPA/JHU) value-added galaxy catalog (Brinchmann et al. 2004),[10] and (4) cross-correlation with the NASA Extragalactic Database (NED). Green et al. (2009) and Constantin et al. (2009) give details on

[7] ChaMP results and data are available online: http://hea-www.harvard.edu/CHAMP.

[8] A list of the *Chandra* fields included in this study (obsid, R.A., decl., exposure time (ks), number of ChaMP/SDSS matches, and total number of optical spectra) can be found at http://hea-www.cfa.harvard.edu/CHAMP/.

[9] The brightest ChaMP fluxes are $\sim f_x(0.5\text{–}8.0\ \mathrm{keV}) \sim 5 \times 10^{-13}$ erg cm^{-2} s^{-1}, where the flux limit represents the number of counts detectable in 90% of simulation trials, converted to flux assuming a power-law $\Gamma = 1.7$ at $z = 0$ and the Galactic N_H appropriate for each obsid.

[10] Publicly available at http://www.mpa-garching.mpg.de/SDSS/.

matching the optical spectroscopy with the Extended ChaMP X-ray source catalog.

The Extended ChaMP also includes a comprehensive set of sensitivity maps for ACIS imaging, implemented in the *xskycover* table. This allows (1) recognition of imaged-but-undetected objects, (2) counts limits for 50% and 90% detection completeness, (3) corresponding flux upper limits at any sky position, as well as (4) flux sensitivity versus sky coverage for any subset of obsids. To generate the table, we use the *wavdetect* detection algorithm in CIAO (Freeman et al. 2002) to generate threshold maps at each *wavdetect* kernel scale (1, 2, 4, 8, 16, and 32 pixels). The threshold maps, computed from the local background intensity, determine the magnitude of the source counts necessary for a detection at each pixel with a detection threshold of $P = 10^{-6}$ (corresponding to 1 false source per 10^6 pixels). Thus, when an object is not detected at a given location, the threshold map value serves as an upper limit to the source counts, as normalized via the detailed simulated source-retrieval results of Kim et al. (2007b). The *xskycover* table covers the full Extended ChaMP with sky pixels, each $10' \times 10'$, whose boundaries are chosen to match a regular commensurate grid across the sky. The final sensitivity in any given sky pixel is interpolated from the two threshold maps computed at scales that bracket the size of the point-spread function (PSF) at that location (for additional details, see the appendix to Green et al. 2009). The accuracy of the *xskycover* counts limits for 50% and 90% detection completeness were verified by Aldcroft et al. (2008) using the Chandra Deep Field South (CDF-S).

2.2. The Sloan Digital Sky Survey

The SDSS is an extensive photometric and spectroscopic optical survey that covers nearly one-quarter of the northern sky (Stoughton et al. 2002; Abazajian et al. 2003, 2004, 2005; Adelman-McCarthy et al. 2006, 2007, 2008). With a dedicated 2.5 m telescope, the SDSS accomplishes uniform photometry in five filters (u, g, r, i, z) to magnitudes as faint as $r < 22.5$, with astrometric uncertainty similar to *Chandra*'s (i.e., better than $0\farcs1$ for $r < 20.5$; Pier et al. 2003). The SDSS data pipeline analyzes object morphology and provides reliable star–galaxy separation to $r \sim 21.5$ (Lupton et al. 2002; Scranton et al. 2002). During its main survey phase (through DR7), the SDSS has obtained photometric measurements for over 350 million unique objects. The SDSS also employs a pair of dual multiobject fiber-fed spectrographs, and has obtained spectra for ∼900,000 galaxies, ∼120,000 quasars, and ∼450,000 stars.[11]

For the present study, we query SDSS DR5 (Adelman-McCarthy et al. 2007), i.e., imaging and spectroscopy taken through 2005 July 1, which includes photometry for 217 million objects over 8000 deg^2 and about 1 million spectra of galaxies, quasars, and stars chosen from 5713 deg^2 of the imaging data. By selecting SDSS data within $20'$ of each *Chandra* aim point (or within $28'$ where the expansion yielded additional high-confidence matches), we create a ChaMP/SDSS catalog of objects within the 323 *Chandra* obsids described above. A photometric recalibration effort for the SDSS Data Release 6 (DR6), resulted in improvements to the SDSS photometric zero points (Adelman-McCarthy et al. 2008; Padmanabhan et al. 2008). We thus cross-correlate our DR5 ChaMP/SDSS catalog with the DR6 to utilize these "UberCal" magnitudes. As mentioned above, we also cross-correlate our ChaMP/SDSS catalog with the new SDSS DR7 spectroscopic database to obtain the largest, most up-to-date spectroscopic sample.

3. SAMPLE SELECTION

To create a high-quality optical galaxy sample with an X-ray flux (or flux limit) for each object, we apply a series of X-ray and optical selection criteria to the ChaMP/SDSS sample. Our sample-selection logic is summarized in Figure 1 and described in detail below.

3.1. X-ray and Optical Quality Cuts

As described in Section 2.1, the Extended ChaMP contains 392 unique *Chandra* fields, 323 of which fall within the SDSS DR5 footprint. The catalog of SDSS objects recovered within this overlap region contains 980,214 individual SDSS objects; we refer to this as our "Parent" sample.

To insure the deepest and most uniform X-ray coverage, we exclude area from the ACIS-S S4 chip (`CCD 8`) which sustained damage early in the *Chandra* mission and has high background and streaking as a result. We accept only area with off-axis angles (OAA) $< 12'$—at larger OAAs the PSF broadens considerably and becomes distorted (Feigelson et al. 2002; Kim et al. 2007a), which leads to large uncertainties in centroiding and source counts. We also exclude area near ACIS chip edges and in chip gaps where the exposure times are significantly shorter. To enforce this criterion, we require that the effective exposure time at each *xskycover* sky pixel be greater than 80% of the maximum exposure time for the obsid. These X-ray quality cuts reduce our X-ray sky coverage to ∼26 deg^2.

In a number of the *Chandra* fields, the SDSS DR5 data do not cover the full obsid. To crudely quantify the optical coverage of our X-ray fields, we perform visual inspection of the 323 ChaMP/SDSS overlap obsids and assign a coverage fraction to each. An estimate of the sky area based on these rough coverage fractions is approximately 21 deg^2 and is a lower limit to our actual joint ChaMP–SDSS coverage. The SDSS catalog associated with this sky coverage area contains 483,940 objects (∼49% of the Parent sample).

For the X-ray-detected subset of the galaxy sample, we apply additional quality constraints. All X-ray-detected objects in the ChaMP survey area are visually inspected, wherein we overplot X-ray centroids and their associated positions on both the X-ray and optical images to identify poorly matched, multiply matched, or photometrically contaminated objects. We accept only objects with the highest-confidence, uncontaminated matches, i.e., a single optical counterpart with an X-ray-to-optical position offset not greater than $2''$ and/or less than the 95% X-ray position error. Match statistics for the X-ray detections in the Extended ChaMP catalog are described in detail in Covey et al. (2008) and Green et al. (2009). We also eliminate X-ray sources that most likely result from (or have possibly been affected by) cosmic-ray afterglows. The sources rejected by this set of ChaMP quality cuts decrease our sample by less than 1%.

An accurate AGN fraction requires a clean sample of both X-ray detections and non-detections. We thus also remove photometric contaminants from our optical sample using the "flags" included in the SDSS photometric catalogs.[12] We include only unsaturated, `PRIMARY` (mode = 1) objects that are classified as either a star (type = 3) or a galaxy (type = 6) and whose five-band photometry is without error codes ($u, g, r, i, z > 0$). To

[11] See http://www.sdss.org for additional details and public data access.

[12] See http://www.sdss.org/dr7/products/catalogs/flags.html for a detailed description of the SDSS image processing flags.

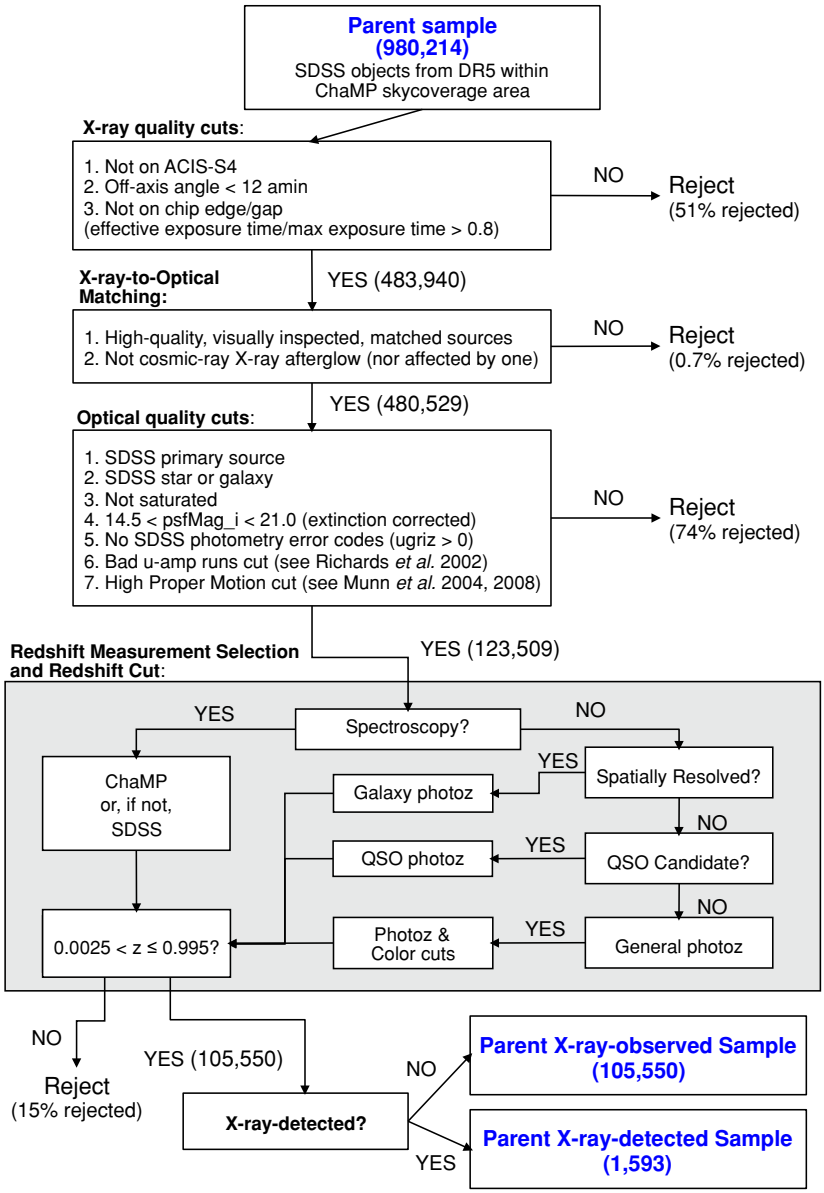

Figure 1. Decision tree showing the sample-selection criteria for clean samples of SDSS objects within the ChaMP sky coverage area for which *Chandra* X-ray flux limits can be assigned, and for *Chandra* X-ray detections. We refer to these as the "Parent X-ray-observed" and "Parent X-ray-detected" samples, respectively.
(A color version of this figure is available in the online journal.)

avoid poor photometry both at the bright and faint extremes of the survey, and to insure uniform coverage at the faintest fluxes, we select objects with *i*-band psf-magnitudes between 14.5 and 21.0. We also eliminate objects impacted by bad *u*-amplifier runs (Richards et al. 2002).

As described in Section 2.2, the SDSS pipeline provides reliable star–galaxy separation for objects down to $r \sim 21.5$. This distinction is a morphological one, and thus cannot correctly characterize active galaxies and quasars that appear to be point sources without consulting optical color information. Faint objects at high redshift are also likely to be misclassified by morphological diagnostics. Eliminating all SDSS "stars" would thus bias our overall fraction. As a result, we do not remove point sources a priori from our sample. Instead, we eliminate stars based on their proper motions, positions in SDSS color–color and color–magnitude diagrams, and spectroscopic or photometric redshifts. (See Section 3.2 for a description of our color and redshift cuts.)

Munn et al. (2004, 2008) have published a proper motion catalog that combines USNO-B and SDSS observations. We use the Munn catalog to assign proper motions to our catalog objects where there is a single USNO-B match within 1″ (match = 1), the rms fit residuals (sigRa, sigDec) are less than 350 mas in each coordinate, and there is at least one USNO-B detection and one SDSS detection per source (nfit > 2). To eliminate high proper motion objects (i.e., stars), we require that the proper motion in at least one coordinate be larger than 3σ, where σ is the proper motion uncertainty in that coordinate (e.g., $|\mathrm{PM_{RA}}| \geqslant 3 \times \sigma_{\mathrm{RA}}$), and that the total proper motion be larger than 11 mas yr^{-1}.

The combined X-ray and optical quality cuts described in this section result in a catalog of 123,509 SDSS objects.

3.2. Redshift and Color Selection

To assign a redshift to each object in our Parent sample, we exploit both spectroscopic and photometric redshift catalogs. We select a *bestz*, the highest quality redshift available, by ranking

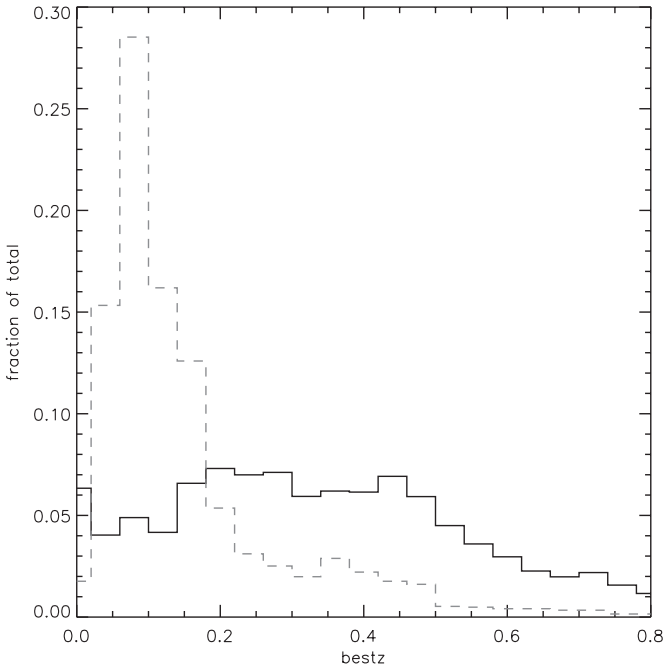

Figure 2. Fractional histogram of the best redshift for the "Full" sample (105,550 galaxies; black solid line) and the spectroscopic sub-sample (2668 objects from ChaMP and SDSS DR7 spectroscopy; gray dashed line). The Full sample contains redshifts to $z \sim 1$, where the photometric redshifts become less reliable, while the spectroscopic sub-sample shows a strong peak at low redshift, $0.05 < bestz < 0.1$. The peak in the spectroscopic sub-sample results largely from SDSS spectroscopic selection criteria.

Table 1
SDSS Photometric Redshifts

Catalog	*Photoz*	*Photoz2*
Number	33,693	68,908
Source type	Unresolved	Resolved
Method	Template fitting	Neural network
Abbreviation	Template	NN
Reference	Csabai et al. (2003)	Oyaizu et al. (2008)

the redshift catalogs as follows: (1) the ChaMP spectroscopic catalog (398 objects; Green et al. 2004), (2) the SDSS DR7 spectroscopic catalog (2270 objects; Abazajian et al. 2009), (3) the SDSS neural network (NN) *Photoz2* catalog for resolved objects (68,908 objects; Oyaizu et al. 2008), (4) the DR6 Quasar Photometric Redshift Catalog (281 objects; Richards et al. 2009), and (5) for unresolved point sources with no other redshift determination, the DR6 version of the SDSS *Photoz* catalog, derived from the template-fitting method with repaired interpolated templates (33,693 objects; Csabai et al. 2003). Properties of the two SDSS photometric redshift catalogs, *Photoz* and *Photoz2*, are summarized in Table 1. We choose the DR6 version of the SDSS *Photoz* catalog (henceforth, the "point source template" or "template" photo-z) because it contains photometric redshift estimates for point sources that are not included in the other catalogs; e.g., the newer DR7 catalog is limited to objects classified morphologically by the SDSS pipeline as galaxies (Abazajian et al. 2009). Based on our selection scheme, only objects with stellar morphology are assigned point source template photo-z's. We eliminate all spectroscopically confirmed stars from our sample.

Figure 2 shows normalized histograms of the redshifts for our "Full" sample (solid black line) and for the spectroscopic

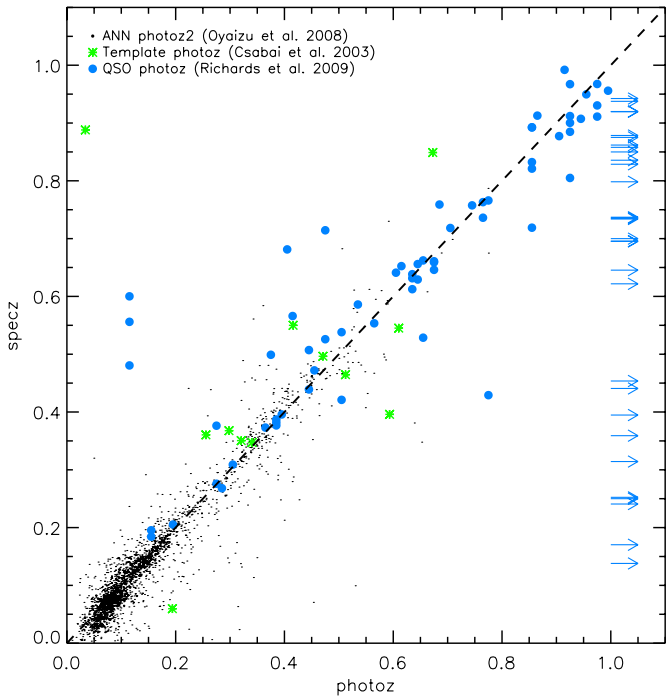

Figure 3. Spectroscopic redshift vs. photometric redshift for 2668 objects in our galaxy sample with spectroscopy (398 from ChaMP and 2270 from SDSS DR7). The symbol type represents the photometric redshift catalog used: the SDSS DR6 resolved NN photo-z galaxy catalog (Oyaizu et al. 2008, black points), the SDSS DR6 QSO catalog (Richards et al. 2009, blue filled circles and blue arrows), the SDSS DR6 point source template photo-z catalog (Csabai et al. 2003, green stars). The most prominent photo-z failures at redshifts above $z \sim 1$ are for QSOs (see Section 5.4).

(A color version of this figure is available in the online journal.)

sub-sample (gray dashed line). For those objects with both photometric and spectroscopic redshifts, 97% have $\frac{\Delta z}{(1+z)} < 0.1$ (Figure 3). The photo-z algorithms are the least reliable for quasars (Figure 3, filled circles and arrows). We discuss the impact of these potentially large photometric redshift errors on our determination of the AGN fraction in Section 5.4.

To quote a single error estimate on our *bestz* value, we utilize and/or convert the redshift errors in each catalog into a 1σ Gaussian error. ChaMP spectroscopic redshifts and 1σ redshift errors are estimated via radial velocities, using the cross-correlation and emission-line fitting techniques in the IRAF *rvsao* task (Kurtz & Mink 1998; Green et al. 2004). Redshifts and their errors for the SDSS DR7 spectroscopic sample are estimated using emission-line or cross-correlation techniques.[13]

The Richards et al. (2009) QSO photometric redshift catalog uses a Bayesian approach to estimate a most likely redshift (*zphot*), as well as a high and low redshift (*zphothi* and *zphotlo*) which represent an approximate range for *zphot*, and a probability that *zphot* is within this range. This photometric redshift determination is described in detail by Weinstein et al. (2004). We estimate 1σ errors (i.e., 68% probability intervals) by approximating the *zphot* errors as symmetric and Gaussian. We assume that the *zphothi* and *zphotlo* values bracket the *zphotprob* range for a Gaussian distribution and derive a "1σ" error using Gauss' formula (i.e., using the error function, *erf*). We also utilize the full redshift probability distribution function

[13] A discussion of SDSS redshift determinations is available at http://www.sdss.org/dr7/algorithms/redshift_type.html.

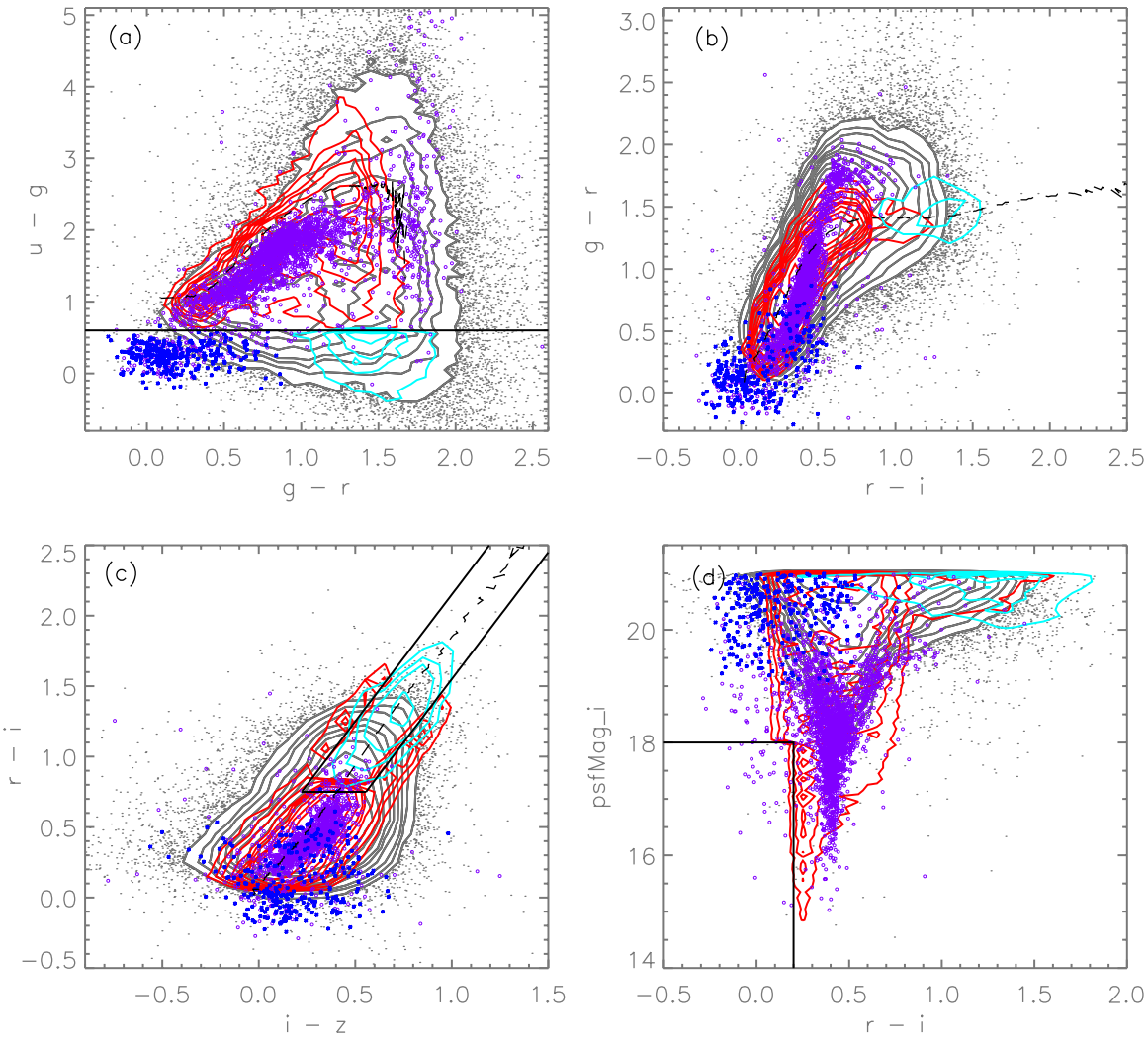

Figure 4. Color–color and color–magnitude diagrams for the Full sample after the cuts described in Section 3.2, and outlined in Figure 1, have been applied to remove galactic (stellar) contaminants, without eliminating extragalactic objects. Gray contours/dots correspond to objects assigned resolved NN photo-z's from the Oyaizu et al. (2008) catalog. Red and cyan contours represent objects that have point source template photo-z's (Csabai et al. 2003) and $(u - g)$ colors above and below 0.6 (panel (a), solid black line), respectively. Dark blue stars indicate objects with QSO photo-z's from Richards et al. (2009). Objects with spectroscopy are indicated with open purple circles. The solid black lines in panels (c) and (d) indicate regions from which red ($(u - g) > 0.6$) point sources with template photo-z's have been eliminated. The black dashed lines in panels (a)–(c) show the SDSS stellar locus from Covey et al. (2007).

(PDF) for the QSO subset in the Monte Carlo (MC) simulations described in Section 5.4.

Both the SDSS resolved NN photo-z and point source template photo-z catalogs include Gaussian 1σ errors, though the methods used to derive them differ. In the resolved NN photo-z analysis, Oyaizu et al. (2008) use a nearest neighbors estimator, with a spectroscopic training set, to determine their best photometric redshift and the associated error. We select their "CC2" values, which employ both magnitudes and concentration indices in the redshift determination. The point source template photo-z catalog uses a template-fitting algorithm with repaired interpolated templates to determine the photometric redshift and associated 68% uncertainty, assuming Gaussian errors (Csabai et al. 2003).

For the sample that has been assigned a point source template photo-z, we make additional color and magnitude cuts to reduce our contamination from stars. We accept all objects for which $(u - g) \leqslant 0.6$ (Figure 4(a), cyan contours), as these are likely to be extragalactic objects associated with a star forming or otherwise active galaxies (see, for example, Richards et al. 2002). For objects with $(u - g) > 0.6$, we remove objects from two regions in color–color and color–magnitude space that are populated primarily by stars (solid black lines, Figures 4(c) and (d)): (1) the first elimination region is defined by SDSS psfMag_i $\leqslant$ 18 and $(r - i) \leqslant 0.2$ and (2) the second is an area along the main-sequence stellar locus in the $(r - i)$ versus $(i - z)$ diagram (parameterized by Covey et al. 2007, black dashed line, Figure 4(c)). For the second cut, we approximate the main-sequence stellar locus as a straight line, described by the formula $(r - i) = 1.8 \times (i - z) + 0.05$. We remove objects with $(r - i) > 0.75$ in a diagonal region within ± 0.3 of the stellar locus center line (solid black lines, Figure 4(c)). We do not cut blueward of $(r - i) = 0.75$, because our spectroscopic sample (open purple circles), which consists of galaxies and AGN only, indicates that this would begin to remove galaxies from our sample. Despite our efforts to eliminate stellar point sources, our sample is still likely to suffer from considerable stellar contamination. We discuss and quantify the impact of this contamination on our AGN fraction in Section 5.5.

Once a *bestz* has been assigned and the most likely stellar contaminants have been removed, we restrict our attention to those objects with $0.0025 < bestz < 0.995$. This redshift cut

avoids cases where the photometric errors are large and/or the photometric redshift algorithms cannot find a suitable fit. These redshift, color, and spectroscopic cuts remove another ∼15% of the sample, leaving 105,550 objects in our optical galaxy catalog—the "Parent X-ray-observed" sample. Of these, 1593 are X-ray detected—these form our "Parent X-ray-detected" sample. (As a result of this selection scheme, the objects in the X-ray-detected sample are a subset of those in the X-ray-observed sample.) These objects are shown in the color–color and color–magnitude diagrams of Figure 4: ChaMP/SDSS spectroscopic redshifts (open purple circles), QSO photometric redshifts (dark blue stars), resolved NN photo-z galaxies (gray contours), the point source template photo-z population with $(u - g) \leqslant 0.6$ (cyan contours), and the point source template photo-z population with $(u - g) > 0.6$, which also meet the color cuts described above (red contours).

4. DERIVED PROPERTIES AND VOLUME-LIMITED SAMPLES

4.1. Galaxy Properties

We calculate optical k-corrections and absolute magnitudes using `kcorrect v4_1_4` (Blanton & Roweis 2007), via the relation

$$m_R = M_Q + \mathrm{DM}(z) + K_{\mathrm{QR}}(z) - 5\log h, \quad (1)$$

where m_R is the apparent magnitude, M_Q is the absolute magnitude, $\mathrm{DM}(z) = 25 + 5\log[D_L/(h^{-1}\ \mathrm{Mpc})]$ is the distance modulus calculated from the luminosity distance D_L, and $K_{\mathrm{QR}}(z)$ is the k-correction (Hogg et al. 2002). In particular, we use `sdss_kcorrect` and input our *bestz*, extinction-corrected SDSS model magnitudes, and model-magnitude errors. Since the `kcorrect` algorithm assumes a Hubble constant $H_0 = 100\,h$ km s^{-1} Mpc^{-1} with $h = 1$, we also convert to $h = 0.7$. The resulting i-band k-corrections (to rest-frame $z = 0$) and absolute magnitudes, M_i, are shown as a function of *bestz* in Figure 5. We identify spectroscopic absorption line galaxies (ALGs; red stars) and narrow emission-line galaxies (NELGs; cyan stars) based on their MPA/JHU line classifications. The spectroscopic sub-sample appears at the bright end of the absolute magnitude distribution, as expected from SDSS main galaxy sample target selection algorithm which requires an r-band Petrosian magnitude brighter than 17.77. In the top panel of Figure 5, the ALGs follow a tighter trend in k-correction than their emission-line counterparts. This trend is also expected, since emission-line strengths vary widely in star-forming galaxies and AGNs. We indicate objects with QSO photometric redshifts (blue filled circles) and note that in many cases their k-corrections (and resulting M_i) lie far from the main galaxy locus. We test the impact of this bias on our fractions in Section 5.4 and discuss its source in Section 5.5.

In the bottom panel of Figure 5, we color-code the points by the redshift catalog from which they originate (red and cyan symbols as in the top panel for spectroscopic redshifts, blue filled circles for QSO photo-z's, light gray points for the resolved NN photo-z catalog, and green points for the point source template photo-z catalog). There are several noticeable structures at the bright end of the M_i versus *bestz* relation. The most prominent of these results from the Ca H-K 4000 Å break passing between the SDSS g and r filters (see, for example, Figure 1 of Padmanabhan et al. 2007). We estimate the edges of this "gap" at 5200 Å and 5700 Å and mark the redshift corresponding to observed-frame 4000 Å as black vertical bars. In this rendering of the

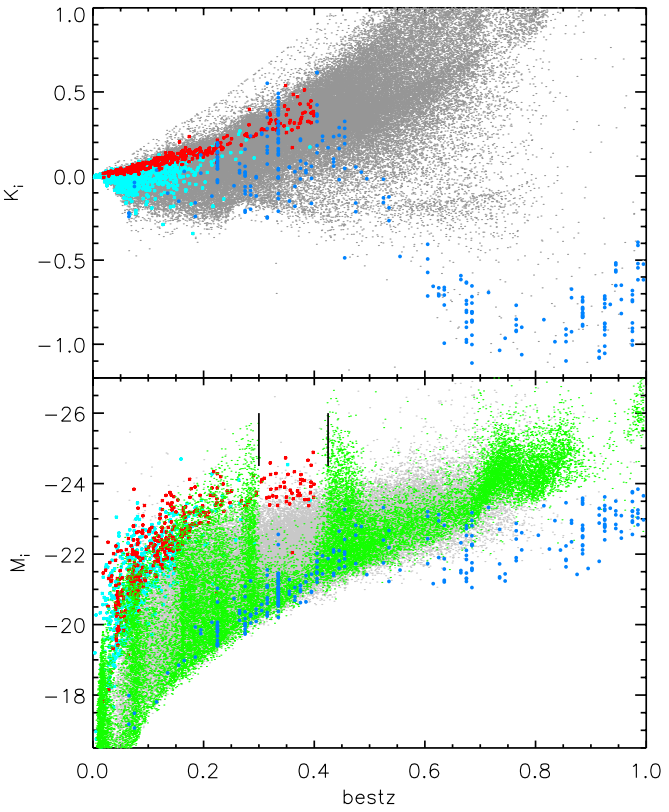

Figure 5. Top: k-correction as a function of *bestz* for the Full galaxy sample (gray points). Objects with spectroscopic classifications from the DR7 MPA/JHU catalog are marked (red stars for absorption line galaxies, cyan stars for narrow emission-line galaxies), and objects with QSO photometric redshifts (blue filled circles) are also overplotted for comparison. Bottom: absolute magnitude as a function of *bestz*, determined after the k-correction from the top panel has been applied. The light gray points indicate objects assigned a resolved NN photo-z and the green points are those with a point source template photo-z (i.e., the sum of the red and cyan contours in Figure 4); the remaining symbols are as in the top panel. The prominent structures at *bestz* ∼0.3 and 0.43 result from the 4000 Å Ca H–K break passing between the SDSS g and r filters (see, e.g., Padmanabhan et al. 2007). We estimate the edges of this filter gap at 5200 Å and 5700 Å and mark the redshift corresponding to observed-frame 4000 Å as black vertical lines.

data, we see that most of the structure comes from the point source template photo-z objects, which are, by definition, red point sources ($(u - g) > 0.6$) in the SDSS. That the point source template photo-z catalog does not perform well for these objects is not a surprise since its primary spectroscopic training sets are the SDSS main galaxy sample and the luminous red galaxy sample.

Using the ChaMP's X-ray sensitivity maps (see description of the *xskycover* table in Section 2.1), we assign a *Chandra* broadband (0.5–8.0 keV) X-ray flux limit to each of the galaxies in our X-ray-observed sample. We also assign a broadband X-ray flux to each detection. With these X-ray fluxes (and flux limits), we calculate the X-ray-to-optical flux ratio, à la Hornschemeier et al. (2000), using the SDSS r-band apparent model magnitudes:

$$\log(f_x/f_{r'}) = \log f_x(0.5\text{–}2\ \mathrm{keV}) + 5.57 + (r'/2.5), \quad (2)$$

where the conversion constant is determined assuming $f(\nu_0) = 3.631 \times 10^{-20}$ erg cm^{-2} s^{-1} Hz^{-1} and using the SDSS r'-band effective wavelengths (Fukugita et al. 1996). We also use the *bestz*, together with ChaMP X-ray fluxes and flux

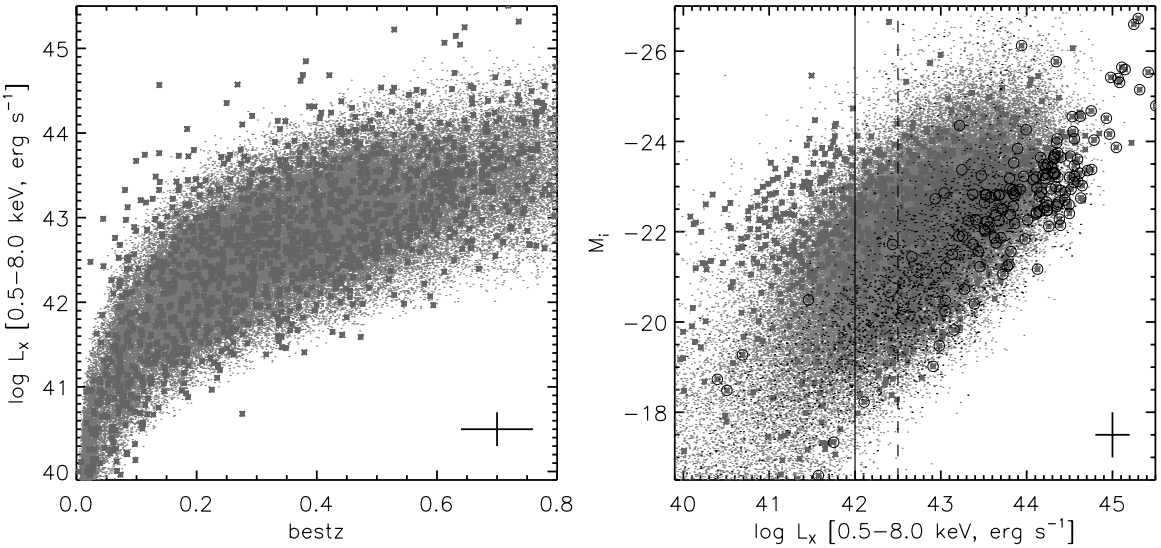

Figure 6. Left: log of the broadband (0.5–8.0 keV) X-ray luminosity, log L_X, as a function of *bestz* for the X-ray-observed (light gray points) and X-ray-detected samples (dark gray stars). Right: absolute *i*-band magnitude vs. log L_X (gray symbols as in the left panel). The solid line marks log $L_X = 42$, the limiting X-ray luminosity used for our AGN fraction calculations; the dashed line indicates log $L_X = 42.5$, the limit used for AGN fraction calculations in the zCOSMOS survey (Silverman et al. 2009a). The black points (upper limits) and large, black open circles (detections) mark objects that reside off the main locus in the M_i vs. host mass diagram (see Figure 14 and Section 5.5). Representative 1σ error bars are plotted in the lower right corner of both panels. These are the median uncertainties for the X-ray-observed sample, derived from the 100-iteration "full" Monte Carlo simulation described in Section 5.4—the error bars thus derive only from uncertainties in the redshifts.

limits, to calculate luminosity distances[14] (D_L), broadband X-ray luminosities (L_X) for detections, and X-ray luminosity limits ($L_{X,\rm lim}$; 90% confidence in the broad band; Aldcroft et al. 2008) for non-detections. In Figure 6, we show log L_X (dark gray stars) and log $L_{X,\rm lim}$ (light gray points) in units of erg s^{-1}. On the left, the X-ray luminosities (limits) are shown as a function of *bestz*—the X-ray detections span the locus of optical galaxies uniformly, indicating that our optical selection has not introduced obvious selection biases in the X-ray. On the right, we show M_i versus log L_X (or log $L_{X,\rm lim}$) and mark two luminosity limits, log $L_X = 42$ and log $L_X = 42.5$, which we employ later in calculating our field AGN fraction and comparing our results to those of deep-field surveys.

Assuming an optical continuum power-law slope of $\alpha = -0.5$ ($f_\nu \propto \nu^\alpha$, where ν is the emission frequency), we derive rest-frame monochromatic optical luminosities at 2500 Å ($l_{2500\,\text{Å}}$; erg s^{-1} Hz^{-1}) using the SDSS *g*-band dereddened magnitude. In theory, the *u*-band magnitude would be more appropriate for objects with *bestz* < 0.53, because the filter's central wavelength is closer to $(1+z) \times 2500$ Å, but the large errors on *u*-band magnitudes mitigate this improvement. We derive the 2 keV luminosity ($l_{2\,\text{keV}}$; erg s^{-1} Hz^{-1}) from the broadband flux using PIMMS and assuming an unabsorbed power law with spectral slope $\Gamma = 1.7$. The slope of a hypothetical power law from 2500 Å to 2 keV is commonly characterized by $\alpha_{\rm ox}$, where $\alpha_{\rm ox} = 0.3838 \times \log(l_{2500\,\text{Å}}/l_{2\,\text{keV}})$; we plot $\alpha_{\rm ox}$ as a function of $l_{2500\,\text{Å}}$ in Figure 7.

4.2. Volume-limited Samples

Using these derived properties, we define five samples complete in *bestz* and M_i (referred to as volume-limited samples hereafter) to calculate our X-ray-active and AGN fractions. We note that this makes ours an optically selected, X-ray-detected (or limited) study. The five volume-limited samples shown in Figure 8 are defined as (1) $z \leqslant 0.125$ and $-18 \geqslant M_i > -20$, (2) $z \leqslant 0.275$ and $-20 \geqslant M_i > -21$, (3) $z \leqslant 0.4$ and $-21 \geqslant M_i > -22$, (4) $z \leqslant 0.55$ and $-22 \geqslant M_i > -23$), and (5) $z \leqslant 0.7$ and $M_i \leqslant -23$. (The low-redshift limit for all samples is $z = 0.0025$.) Their constituents are detailed in Table 2.

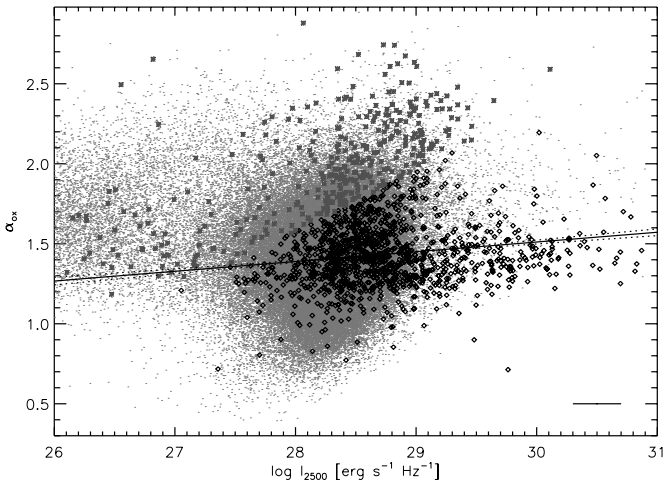

Figure 7. $\alpha_{\rm ox}$ vs. optical (2500 Å) luminosity for the Full galaxy sample. X-ray-observed galaxies are shown as light gray points, X-ray detections are marked with large symbols according to their broadband X-ray luminosity: log $L_X \geqslant 42$ (black diamonds) and log $L_X < 42$ (dark gray stars). The ChaMP QSO best-fit regression line ($\alpha_{\rm ox} = (0.061 \pm 0.009)\log(l_{2500\,\text{Å}}) - (0.319 \pm 0.258)$) from Green et al. (2009) is shown as a black solid line with errors. Representative 1σ error bars are as described in Figure 6; the median error bar for the $\alpha_{\rm ox}$ is smaller than the width of the horizontal line for the $\log(l_{2500\,\text{Å}})$ error bar.

We determine each galaxy's stellar mass via the `kcorrect` tool, which generates the coefficients of a fit between a galaxy's spectral energy distribution (SED) and a set of template spectra. Blanton & Roweis (2007) derive five global templates from 450 instantaneous bursts of star formation from Bruzual & Charlot (2003) spectral synthesis models, using the Chabrier (2003) stellar initial mass function and the Padova 1994 isochrones,

[14] Luminosity and comoving distances are calculated using the Python version of the Wright Cosmology Calculator (Wright 2006).

Table 2
Volume-limited Samples

S	*bestz*	M_i		Full		Spec	
	Max	Min	Max	$N_{\rm det}$	$N_{\rm lim}$	$N_{\rm det}$	$N_{\rm lim}$
1	0.125	−18	−20	29	5028	2	182
2	0.275	−20	−21	88	10949	7	342
3	0.400	−21	−22	239	17984	37	566
4	0.550	−22	−23	416	22095	68	567
5	0.700	−23	...	323	13628	57	464

Notes. Properties of the five volume-limited samples for the Full galaxy catalog (described in Section 4.2 and shown in Figure 8) and the spectroscopic sub-sample. The first column gives the sample number; the second gives the maximum redshift (*bestz*; all samples have a minimum *bestz* = 0.0025); the third and fourth give the absolute SDSS *i*-band magnitude range; and the remaining columns contain the number of X-ray-detected and X-ray-observed optical galaxies.

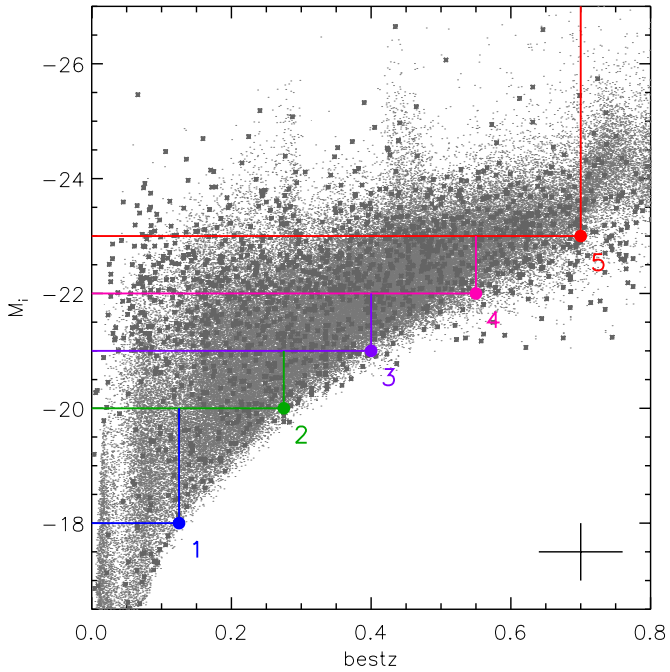

Figure 8. Absolute *i*-band magnitude vs. *bestz* for the 105,550 galaxies in the X-ray-observed sample (light gray points) and the 1593 X-ray-detected sources (large dark gray stars). Colored lines and large symbols/numbers indicate the five independent, volume-limited samples (see Section 4.2 and Table 2) for which we determine the X-ray-active and AGN fractions. Representative 1σ error bars are as described in Figure 6.

(A color version of this figure is available in the online journal.)

and 35 templates from MAPPINGS-III (Kewley et al. 2001) models of emission from ionized gas. These global templates are characterized using "non-negative matrix factorization," which determines a set of non-negative templates that can be combined linearly to explain a data set. The five global templates correspond roughly to a very old galaxy template spectrum, a very young template, and several intermediate templates (see Figure 4 in Blanton & Roweis 2007). The `kcorrect` template fits can be interpreted physically and we utilize them to determine mass estimates for each of our galaxies. We sum the fit coefficients (units: $1\,M_\odot/(D_L/10\ {\rm pc})^2$, where D_L is the luminosity distance) and multiply by $(D_L/10\ {\rm pc})^2$ to find the total current stellar mass for each galaxy. In the left panel of Figure 9, we plot log $M_\star$, in units of solar mass, as a function of *bestz*; on the right we show rest-frame $(u-r)_0$ versus log $M_\star$. To compare with studies that use mass to define their galaxy samples (e.g., Silverman et al. 2008, 2009a, 2009b), we create complete mass samples, denoted samples 1*–5*, analogous to those in Figure 8: $9 \leqslant \log M_\star < 9.8$, $9.8 \leqslant \log M_\star < 10.4$, $10.4 \leqslant \log M_\star < 11$, $11 \leqslant \log M_\star < 11.6$, and $\log M_\star \geqslant 11.6$ (the redshift intervals are unchanged). These mass intervals are selected based on a crude correspondence between M_i and log $M_\star$, i.e., 1 mag in M_i is roughly equivalent to 0.4 dex in log $M_\star$ (see also Figure 14).

5. THE FRACTION

5.1. The X-ray-active Fraction

We calculate the fraction of X-ray-active galaxies for each of the five samples complete in *bestz* and M_i described in Section 4.2. In addition to the optical criteria, we apply X-ray selection criteria so that our samples are complete in both the optical and X-rays. For each fraction, we define an X-ray threshold, L'_X, which gives the brightest X-ray luminosity to which all objects in the sample are, or would have been, detected by *Chandra*. Any *detected* source in the sample must have an X-ray luminosity at or above the X-ray luminosity limit (at the 90% confidence level).

The details of the X-ray criteria are (1) a galaxy appears in the denominator only if its broadband X-ray luminosity upper limit $L_{X,\rm lim}$ (see Section 4.1 for a definition) is less than the chosen threshold, L'_X, regardless of X-ray-detection status. In other words, each optical galaxy counted in the denominator would have been detected at L'_X since $L'_X > L_{X,\rm lim}$, where $L_{X,\rm lim} = 4\pi\, D_L^2\, f_{X,\rm lim}$. (2) The numerator is the X-ray-detected subset of the denominator, where the broadband X-ray luminosity, L_X, for each detection is greater than or equal to the same limiting L'_X used to define the denominator. (We discuss the objects that appear in the volume-limited optical samples, but do not pass the X-ray cut in the Appendix.)

We can express these criteria mathematically with two functions, (1) $G(L_{X,\rm lim}, M_i, bestz)$ to describe galaxies with X-ray luminosity limits, and (2) $X(L_X, L_{X,\rm lim}, M_i, bestz)$ to describe the X-ray detections. We write the denominator and the numerator of the fraction as

$$N_{\rm lim} = \sum_{z_{\rm min}}^{z_{\rm max}} \sum_{M_{\rm faint}}^{M_{\rm bright}} \sum_{0}^{L'_X} G(L_{X,\rm lim}, M_i, bestz), \qquad (3)$$

$$N_{\rm det} = \sum_{z_{\rm min}}^{z_{\rm max}} \sum_{M_{\rm faint}}^{M_{\rm bright}} \sum_{0}^{L'_X} \sum_{L'_X}^{\infty} X(L_X, L_{X,\rm lim}, M_i, bestz), \qquad (4)$$

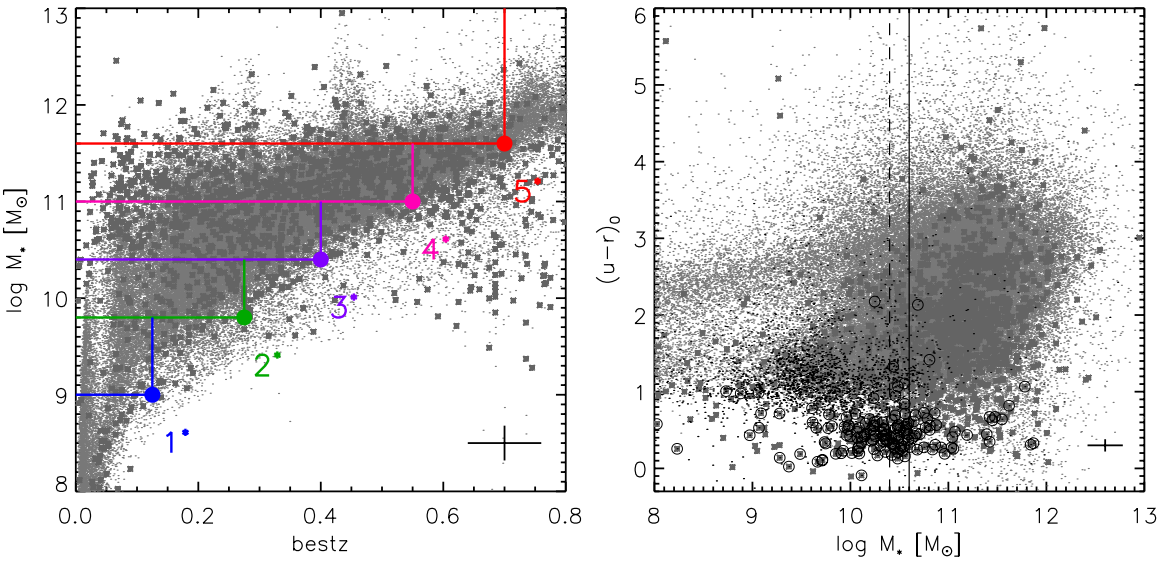

Figure 9. Left: log of the host galaxy mass, log $M_\star$, vs. *bestz* (gray symbols as in Figure 8). A set of samples, complete in galaxy mass, are indicated with colored lines and large symbols/numbers (see Section 4.2). These are analogous to the volume-limited samples in Figure 8. Right: rest-frame $(u-r)_0$ color vs. log $M_\star$ (gray and black symbols as in Figure 6). Black lines mark log $M_\star = 10.6$ (solid) and 10.4 (dashed) and are used to define mass limits for a comparison between our field fractions and those of other X-ray surveys (see Section 6). Representative 1σ error bars in both panels are as described in Figure 6.

(A color version of this figure is available in the online journal.)

where $z_{\rm min}$, $z_{\rm max}$, $M_{\rm faint}$, and $M_{\rm bright}$, define our volume-limited optical samples, and L'_X establishes X-ray completeness. All five volume-limited samples have a minimum redshift $z_{\rm min} = 0.0025$.

Figure 10 shows the X-ray-active fraction as a function of L'_X, where the luminosity threshold is set to the measured L_X for each of the X-ray-detected sources; panels 1–5 show the fraction for the five volume-limited optical samples. Errors on the fraction due to small number statistics, estimated via the β distribution (gray filled circles; see Section 5.2), are largest at the lowest luminosity limits, where both the number of X-ray detections and galaxies is small (see also Figure 18). The sixth panel shows the active fraction over a narrower range of L'_X from all five samples on the same vertical scale (sample 1: blue solid line, sample 2: green dotted line, sample 3: purple dashed line, sample 4: magenta dot-dashed line, sample 5: red triple dot-dashed line). The dashed gray line denotes an X-ray luminosity limit of $L'_X = 10^{42}$ erg s^{-1}, above which we consider our fraction a proper AGN fraction (see Section 5.3), and below which the fraction may be impacted by a mix of stellar emission (principally from X-ray binaries) and hot interstellar medium in the host galaxies.

The redshift distributions of the five optically complete samples differ substantially from one another, see Figure 11. Sample 1 (at the lowest redshifts) shows two peaks, one corresponding to a large number of spectroscopic redshifts at $z = 0.02$ and the other at $z = 0.075$, sample 2 peaks at $z = 0.23$, sample 3 at $z = 0.35$, sample 4 at $z = 0.46$, and sample 5 at about $z = 0.6$. As a result, the increase in X-ray-active fraction between samples 1 and 5 may be due either to a trend with M_i, with z, or with both. We discuss these dependencies in Sections 5.3 and 6.

5.2. Error Estimation via the β Distribution

We face small number statistics throughout this study, particularly when we bin our modest number of X-ray detections further by mass, redshift, color, etc. Statistics used to estimate errors on numbers of events, e.g., the Poisson distribution or the Gehrels (1986) statistic, are not suitable for estimating errors on *fractions*. When it comes to estimating uncertainties on a fraction, one should use the binomial distribution, or its conjugate prior, the β distribution (Evans et al. 2000). Given a fraction, F, and a number of trials, N, the binomial distribution describes the probability of different outcomes. Given the outcome of such a trial, the β distribution describes the probability distribution for the fraction itself. Hence, we determine both the X-ray-active (or AGN) fraction and the uncertainties on the fraction using the regularized incomplete β distribution (see Equation (5) and Figure 12).

The β distribution is continuous, yields a fraction that is well behaved in the extremes where either the numerator or the denominator (or both) are zero, and properly accounts for a numerator and denominator that are not drawn from independent samples, i.e., where one is a subset of the other, as is the case here. We assign a probability distribution to the fraction, P_β (defined on the interval [0, 1]), given the measured values $\alpha = N_{\rm det} + 1$ and $\beta = N_{\rm lim} - N_{\rm det} + 1$. For each input $N_{\rm det}$ and $N_{\rm lim}$, we calculate a cumulative distribution function (CDF) via the β distribution and choose the mean of the CDF as the best value for the X-ray-active fraction, such that

$$F_{\rm mean} = \frac{\alpha}{\alpha + \beta} = \frac{N_{\rm det} + 1}{N_{\rm lim} + 2}. \quad (5)$$

The asymmetric 1σ errors[15] are calculated based on the median value of F (evaluated where $P_\beta = 0.5$), and defined such that $F_{\rm max}$ corresponds to $P_\beta(0.5) + 1\sigma$ and $F_{\rm min}$ corresponds to $P_\beta(0.5) - 1\sigma$ (see Figure 12 for an example). Throughout the remainder of this manuscript (tables excepted), we specify the asymmetric 1σ errors *only* in cases where the upper and lower errors differ by more than 10%; in all other cases we quote the larger of the two. (That is, if we have $F\pm^X_Y$, we will quote $F \pm \max(X, Y)$, unless X and Y differ by more than 10%.) The cumulative X-ray-active fractions and their β distribution errors,

[15] We take $1\sigma = 0.34134$.

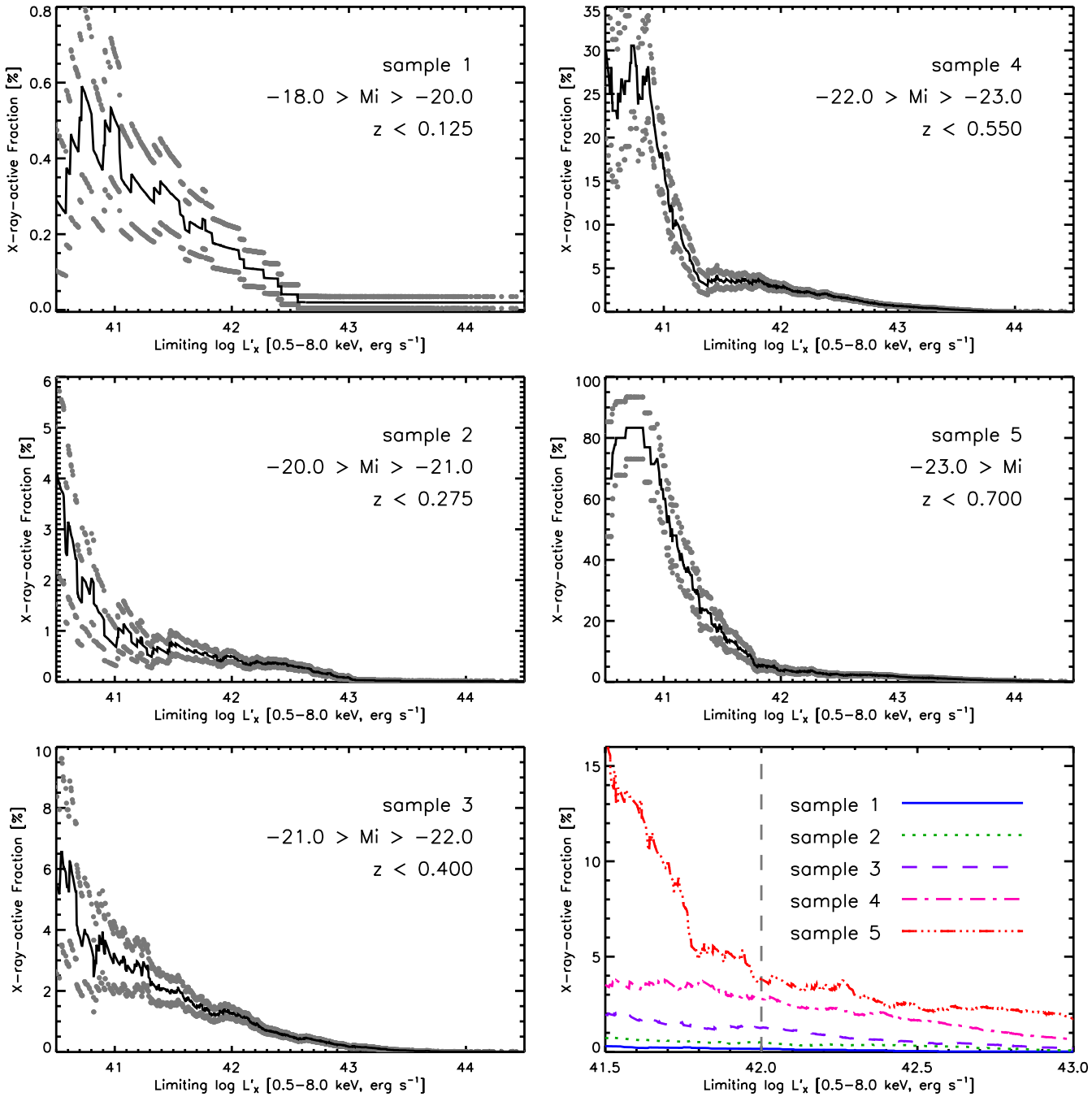

Figure 10. First five panels show the X-ray-active fraction as a function of limiting broadband X-ray luminosity for each of the five volume-limited samples described in Table 2 and shown in Figure 8. The solid lines connect the fraction as determined for the limiting L'_X at each X-ray detection in the sample. The 1σ errors (determined via the β distribution; see Section 5.2) appear at each point where an active fraction was calculated. The final panel contains the best value for the fraction for each sample, plotted on the same scale for ease of comparison: sample 1 (solid blue line), sample 2 (dotted green line), sample 3 (dashed purple line), sample 4 (dot-dashed magenta line), and sample 5 (triple dot-dashed red line). The dashed gray line in this last panel denotes the limiting X-ray luminosity, $\log L_X = 42$, that we associate with AGN; at this limit the AGN fractions are $F_{\rm AGN,1} = 0.16\% \pm 0.06\%$, $F_{\rm AGN,2} = 0.50\% \pm 0.11\%$, $F_{\rm AGN,3} = 1.27\% \pm 0.18\%$, $F_{\rm AGN,4} = 2.85\% \pm 0.39\%$, and $F_{\rm AGN,5} = 3.80\% \pm 0.92\%$ for samples 1–5, respectively (see also Table 3).

(A color version of this figure is available in the online journal.)

for a set of seven useful X-ray luminosity thresholds, appear in Table 3.

5.3. The AGN Fraction

In this section and the discussion that follows, we differentiate between the X-ray-active fraction, which can be defined for an arbitrary L'_X threshold, and the AGN fraction, $F_{\rm AGN}$. For our purposes, the AGN fraction will refer only to the cases where the limiting X-ray threshold is $L'_X = 10^{42}$ erg s^{-1}, a typical cutoff for AGN activity (Zezas et al. 1998). For each of our volume-limited samples, we measure the following AGN fractions (see also Table 3, bold entries): $F_{\rm AGN,1} = 0.16\% \pm 0.06\%$, $F_{\rm AGN,2} = 0.50\% \pm 0.11\%$, $F_{\rm AGN,3} = 1.27\% \pm 0.18\%$, $F_{\rm AGN,4} = 2.85\% \pm 0.39\%$, and $F_{\rm AGN,5} = 3.80\% \pm 0.92\%$.

To test for evolution in the AGN fraction with *bestz*, and/or a change with M_i or galaxy mass, we further subdivide our five volume-limited samples, recalculate the AGN

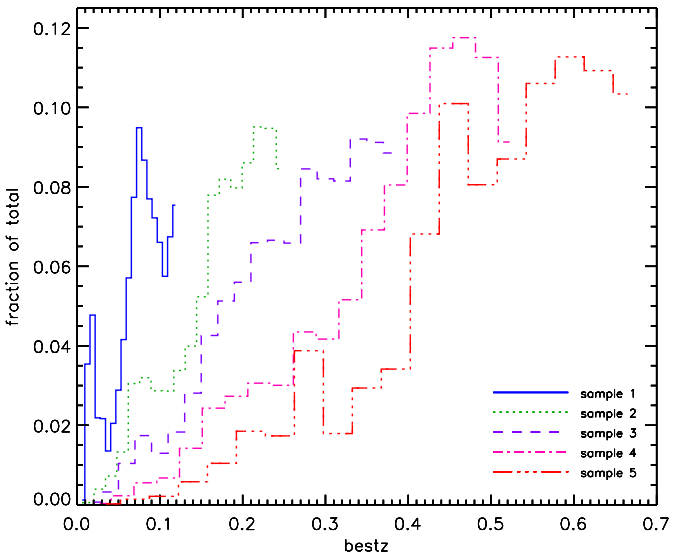

Figure 11. Distribution of *bestz* for each of the five samples described in Table 2 and in Figure 8 (line styles are as in the bottom, right panel of Figure 10).
(A color version of this figure is available in the online journal.)

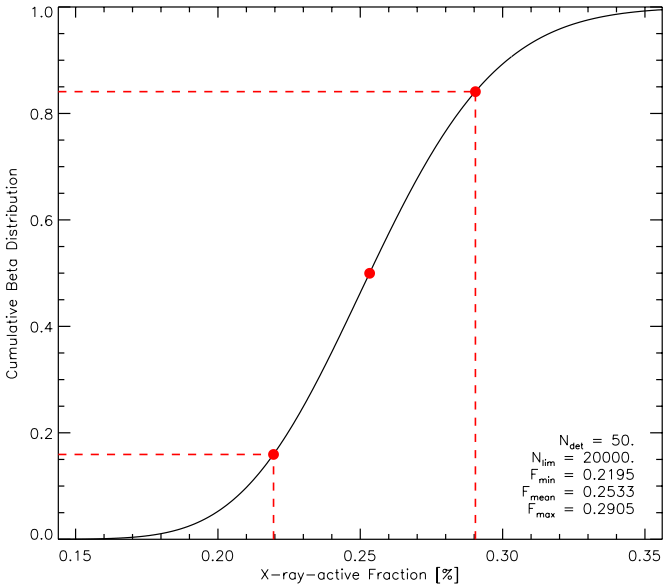

Figure 12. Cumulative β distribution function (black solid line) for a toy example where the number of detections, $N_{\rm det}$, equals 50 and the number of X-ray-observed galaxies, the denominator $N_{\rm lim}$, is 20,000. For these inputs, the mean fraction is 0.25%. The mean value of the CDF, $F_{\rm mean}$, is marked with a large, filled circle, as are the slightly asymmetric 1σ errors (also marked with dashed lines), corresponding to $F_{\rm min}$ and $F_{\rm max}$.
(A color version of this figure is available in the online journal.)

fraction in these finer bins, and perform a Spearman rank correlation analysis (including errors) to assess the significance of any trends. We first sort our data into four absolute magnitude bins, $-20 \geqslant M_i > -21$, $-21 \geqslant M_i > -22$, $-22 \geqslant M_i > -23$, $-23 \geqslant M_i > -24$, and simultaneously fit all 12 of the data points shown in the leftmost panel of Figure 13. We find a marginally significant trend at the ∼76% confidence level between the AGN fraction and *bestz*. In four redshift bins, $z < 0.125$, $0.125 < z < 0.275$, $0.275 < z < 0.4$, and $0.4 < z < 0.55$, we find that the AGN fraction correlates strongly with M_i, at the 91% confidence level (96% if the $0.4 < z < 0.55$ redshift bin is ignored; Figure 13, middle panel). For the same redshift bins, the correlation with galaxy mass is similar, but slightly stronger, ∼93% and 96% with and without the highest-redshift bin (Figure 13, right panel).

These trends reveal a field AGN fraction that increases toward brighter absolute magnitudes and higher masses, as might be expected from cosmological models wherein the merger of massive galaxies fuels both accretion onto a central SMBH and star formation. The weaker evolution of the AGN fraction with redshift indicates that the mechanism for black hole fueling may be changing, e.g., shifting from high-luminosity merger-driven activity to fueling via tidal interactions, bars, dynamical friction, or other lower luminosity drivers (see Martini 2004 for a review). In such a scenario, the lower AGN fraction may reflect the evolution of the AGN X-ray luminosity function, which is characterized by a decrease in accretion luminosity toward the present day. In the leftmost panel of Figure 13, we show two common fits to the AGN X-ray luminosity function (Ueda et al. 2003; Barger et al. 2005; Hasinger et al. 2005), normalized to the mean AGN fraction in the four M_i bins at $z \sim 0.21$: pure luminosity evolution (PLE) $\propto (1+z)^3$ (gray dotted line), and luminosity-dependent density evolution (LDDE) $\propto (1+z)^4$ (dashed gray line). We explore the possibility of an evolving AGN fraction further in Section 6.

5.4. Redshift Monte Carlo Simulations

As discussed in Section 5.2, small number statistics for X-ray-detected sources in our volume-limited bins place a basic limit on our ability to accurately determine the X-ray-active fraction. However, our use of photometric redshifts for the majority of the galaxies (∼97%) in our X-ray-observed sample introduces another potentially large source of error. Photometric redshift errors are of order 3%, but can be as high as 10% at fainter apparent magnitudes (Csabai et al. 2003; Oyaizu et al. 2008). Meanwhile, photometric redshifts for quasars can experience catastrophic failures due to aliasing (Budavári et al. 2001; Richards et al. 2001). Hence, photometric redshift errors dominate the uncertainty on our volume-limited samples. To estimate the impact of the photo-z uncertainties on our active fraction, we perform two MC simulations: a "full" MC and a "quick" MC.

Full MC. In the full MC simulation, the 1σ error for each object not associated with a QSO photometric redshift is multiplied by a normally distributed random number selected from a distribution with a mean of zero and a standard deviation of one. This quantity is added to the best redshift, yielding a new *bestz*.

Since single-valued quasar photometric redshifts, derived using broadband filters, suffer from aliasing in certain redshift regimes they are better described by their full redshift PDF (see, e.g., Myers et al. 2009; Richards et al. 2009, and references therein). Thus, for objects where we have assigned a QSO photometric redshift we use the full redshift PDF, obtained using the nearest neighbor approach of Ball et al. (2008), to calculate the new *bestz*. We also run the MC tests using the QSO 1σ errors described in Section 3.2, instead of the full PDF. The results of those tests show excellent agreement with the MCs that use the QSO PDF. Thus, we do not attempt to acquire full redshift PDFs for all of the objects in our sample.

We use the new *bestz* values for non-QSO and QSO objects to determine new luminosity distances, k-corrections, and absolute magnitudes via `kcorrect`. We then pull five volume-limited samples analogous to those used for our primary analysis using

Table 3
X-ray-active Fraction

$\log L'_X$	$N_{\rm det}$	$N_{\rm lim}$	$N_{\rm det,drop}$	$N_{\rm lim,drop}$	F (%)		
					Min	Mean	Max
Sample 1: $-18 \geqslant M_i > -20$, $bestz \leqslant 0.125$							
41.0	7	1587	7	3441	0.33	0.50	0.68
41.5	8	2974	3	2054	0.20	0.30	0.40
42.0	**6**	**4336**	**0**	**692**	**0.10**	**0.16**	**0.22**
42.5	1	4930	0	98	0.01	0.04	0.07
43.0	0	5026	0	2	0.00	0.02	0.04
43.5	0	5028	0	0	0.00	0.02	0.04
44.0	0	5028	0	0	0.00	0.02	0.04
Sample 2: $-20 \geqslant M_i > -21$, $bestz \leqslant 0.275$							
41.0	2	420	77	10529	0.33	0.71	1.10
41.5	11	1629	57	9320	0.53	0.74	0.94
42.0	**21**	**4415**	**30**	**6534**	**0.39**	**0.50**	**0.60**
42.5	24	7930	7	3019	0.25	0.32	0.38
43.0	7	10240	0	709	0.05	0.08	0.11
43.5	0	10903	0	46	0.00	0.01	0.02
44.0	0	10949	0	0	0.00	0.01	0.02
Sample 3: $-21 \geqslant M_i > -22$, $bestz \leqslant 0.400$							
41.0	8	280	208	17704	2.16	3.19	4.22
41.5	21	1123	164	16861	1.55	1.96	2.36
42.0	**48**	**3860**	**90**	**14124**	**1.09**	**1.27**	**1.45**
42.5	44	9047	42	8937	0.42	0.50	0.57
43.0	23	14507	8	3477	0.13	0.17	0.20
43.5	6	17343	1	641	0.03	0.04	0.06
44.0	0	17949	0	35	0.00	0.01	0.01
Sample 4: $-22 \geqslant M_i > -23$, $bestz \leqslant 0.550$							
41.0	13	83	378	22012	12.49	16.47	20.45
41.5	13	395	356	21700	2.61	3.53	4.44
42.0	**52**	**1857**	**282**	**20238**	**2.47**	**2.85**	**3.24**
42.5	98	6000	155	16095	1.49	1.65	1.81
43.0	86	13209	44	8886	0.59	0.66	0.73
43.5	44	19154	2	2941	0.20	0.23	0.27
44.0	4	21732	0	363	0.01	0.02	0.03
Sample 5: $M_i < -23$, $bestz \leqslant 0.700$							
41.0	11	18	311	13610	49.10	60.00	70.87
41.5	13	84	291	13544	12.34	16.28	20.23
42.0	**15**	**419**	**260**	**13209**	**2.88**	**3.80**	**4.72**
42.5	42	1842	199	11786	1.98	2.33	2.68
43.0	96	5499	88	8129	1.59	1.76	1.94
43.5	94	10085	15	3543	0.85	0.94	1.04
44.0	51	12875	2	753	0.35	0.40	0.46

Notes. The first column gives the broadband (0.5–8.0 keV) X-ray luminosity threshold. The second and third columns contain the number of detections and limits that were used to calculate the mean X-ray-active fraction, $F_{\rm mean}$; columns four and five contain the number of objects that did not pass the X-ray luminosity cut (details in the Appendix). $F_{\rm min}$ and $F_{\rm max}$ are the 1σ upper and lower limits on the X-ray-active fraction (see Section 5.2). The bold rows indicate the AGN fraction, i.e., the fraction for $\log L'_X = 42$.

the new *bestz* and its associated M_i. We adopt the same seven X-ray luminosity thresholds and calculate new X-ray-active fractions for each.

The above constitutes a single iteration of the full MC. The process is computationally expensive; determining the spectral template match and *k*-correction for each of ∼100,000 objects is the largest computational task. Thus, we perform only 100 iterations of the full MC, which result in 100 possible X-ray-active fractions for each volume-limited sample, at each of seven X-ray luminosity limits. We take the median and standard deviation of these fractions and use them to estimate the uncertainty contributed by the photo-z errors. We also use the full MC to estimate the representative error bars shown in Figures 6–9.

Quick MC. In our quick MC simulation, new *bestz* values are derived as in the full MC and new luminosity distances are then calculated. We assume that a small change in the redshift will result in only a small change in the *k*-correction and so leave the *k*-correction unaltered. Hence, the new absolute magnitude is simply the original M_i weighted by the ratio of the luminosity distances: $M_{i,\rm new} = M_i - 5\log(D_{L,\rm new}/D_L)$. We perform this quick MC initially for 100 iterations and make

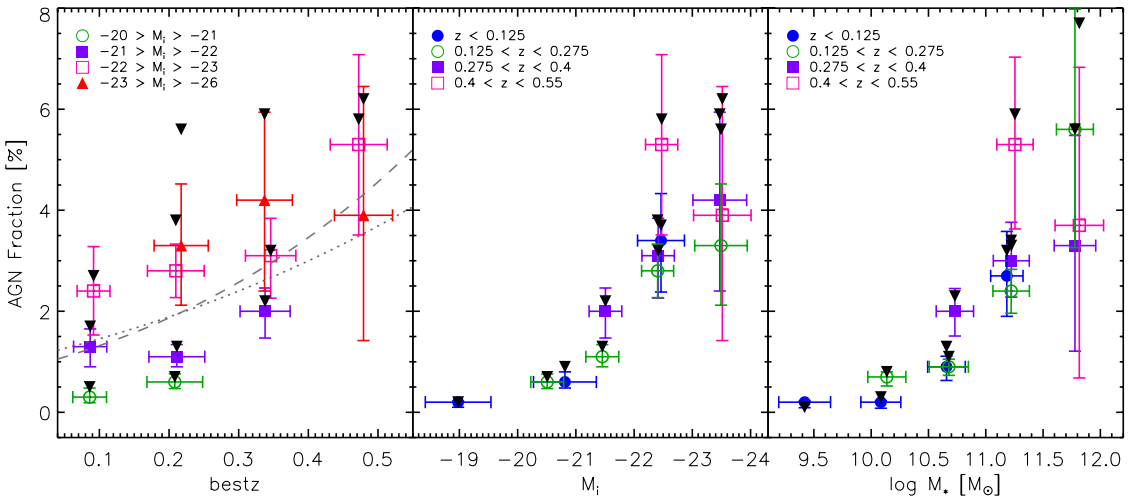

Figure 13. AGN fraction, i.e., $L'_X = 10^{42}$ erg s^{-1}, in bins of redshift (left), absolute i-band magnitude (center), and mass (right). Upper limits on the fractions are plotted as solid, downward-facing black triangles (see Section 5.5 for details). Two common fits for the evolution of the X-ray luminosity function of X-ray-detected AGN, normalized to the mean AGN fraction in the four M_i bins at $z \sim 0.21$, are shown in the left-hand panel: pure luminosity evolution $\propto (1+z)^3$ (gray dotted line), and luminosity-dependent density evolution $\propto (1+z)^4$ (dashed gray line). The Spearman rank correlation test indicates that the active fraction correlates most strongly with galaxy mass (93% confidence; 96% if the $0.4 < z < 0.55$ redshift bin is ignored). There is also a correlation with M_i (91% and 96% confidence, respectively). A weaker correlation with *bestz* is detected at only the 76% confidence level.

(A color version of this figure is available in the online journal.)

a direct comparison to our full MC. We then perform 1000 iterations to achieve more robust statistics. Here again, we derive 100 (or 1000) X-ray-active fractions and compute a median fraction and standard deviation for each volume-limited sample at each of seven X-ray luminosity thresholds.

The errors that result from the redshift MCs are, in general, smaller than the β distribution errors, though in some cases they are of comparable magnitude. For example, if we adopt an X-ray threshold of $L'_X = 10^{42}$ erg s^{-1} for sample 3, the 100-iteration full MC gives a median fraction of $1.25\% \pm 0.12\%$, the 100-iteration quick MC yields a median of $1.25\% \pm 0.11\%$, and the 1000-iteration quick MC gives a median fraction of $1.24\% \pm 0.11\%$. These compare to a β distribution result of $1.27\% \pm 0.18\%$, where the β distribution errors arise from small numbers of X-ray-detected galaxies, instead of photo-z uncertainties. The β distribution and MC errors could be combined in quadrature; or as a conservative estimate, the errors in Table 3 might simply be increased by a factor of $\sqrt{2}$ to take photometric redshift errors into account.

5.5. Selection Effects and Sample Bias

As discussed in Section 3.2, we have included a large number (∼27,000) of red, $(u - g) > 0.6$, point sources in our galaxy sample to insure that we do not bias our AGN fraction at faint apparent magnitudes (and at high redshift) where morphological criteria are less reliable, and to include all possible QSOs. As a result, the denominator of our fractions is likely to be contaminated by stars and the AGN fractions reported here must be taken as a lower limit to the "true" AGN fraction.

To quantify the magnitude of the stellar contamination, we return to SDSS star–galaxy separation (Stoughton et al. 2002). We assume that all of the point sources with red colors ($u - g > 0.6$) *are* actually stars and remove these 27,958 objects along with their X-ray counterparts (120 detections) from our galaxy sample. We re-run our analysis and find mean AGN fractions at $L'_X = 10^{42}$ erg s^{-1} of $0.16\% \pm 0.08\%$ (sample 1), $0.61\% \pm 0.14\%$ (sample 2), $1.53\% \pm 0.33\%$ (sample 3), $3.45\% \pm 0.46\%$ (sample 4), and $5.71\% \pm 1.37\%$ (sample 5). Since some of these excluded objects are certainly galaxies, and the number hosting X-ray-emitting AGN is likely to be smaller than the passive population, we consider these fractions to be upper limits, i.e., we will have eliminated more legitimate galactic objects from the denominator than the numerator. We plot these "maximum" AGN fractions in Figure 13 (filled, black, downward-facing triangles) and note that, with few exceptions, they agree with our original AGN fractions within the errors.

We also consider the possibility that the combination of ChaMP and SDSS spectroscopy (which includes known X-ray sources in its targeting algorithms) introduces a bias in our redshifts, leading to greater spectroscopic completeness in the X-ray-detected sample than in the X-ray-observed sample. This is, at worst, a second-order effect impacting only the precision of the redshifts since we include galaxies in our sample whether or not they have spectroscopy. One exception is along the stellar locus. In regions of the color–color diagram where we have eliminated objects based on their photometric redshifts and colors (see Section 5.5), we do *not* eliminate spectroscopically confirmed galaxies. Thus, we may have an overrepresentation of objects in these particular color regimes due to existing ChaMP and SDSS spectroscopy.

Pollution of the host galaxy light by a central AGN or active star formation is another source of bias in our galaxy sample. Though we are interested in locating active black holes in nearby galaxies, these same sources may contaminate the SED of the host galaxy and thus impact the photometric redshift algorithms and `kcorrect` spectral template matching. There are several possible approaches to this problem: (1) in principle it is possible to correct the host galaxy SED by extrapolating an AGN power-law spectrum, e.g., normalized to the measured X-ray luminosity, into the optical and then subtracting this component. This method is not likely to be efficient for our sample because only a small number (∼1.5%) of our galaxies have X-ray detections. Also, a non-negligible fraction of X-ray AGN have the optical SEDs of normal galaxies (Georgantopoulos & Georgakakis 2005; Hornschemeier et al. 2005; Kim et al. 2006; Civano et al. 2007; Cocchia et al.

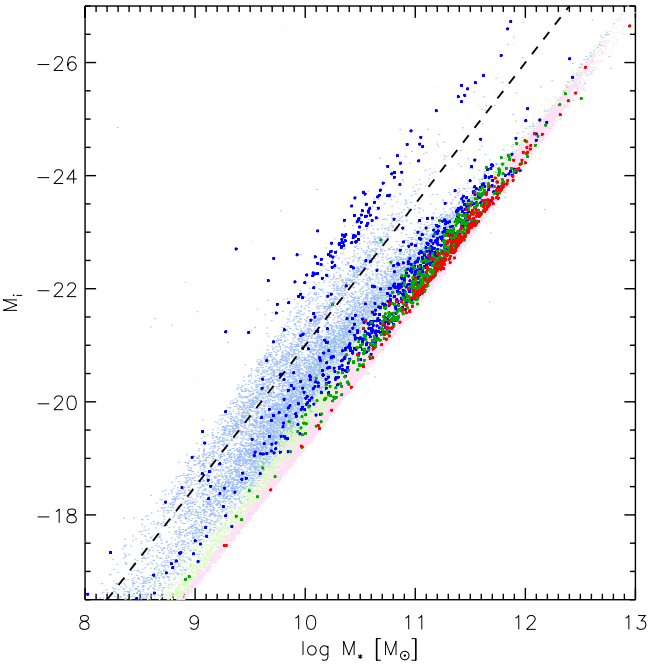

Figure 14. Absolute i-band magnitude vs. log $M_\star$ for the limits (small points) and detections (stars) in the Full galaxy sample. The symbols are colored according to the $(u - r)_0$ criteria described in Section 6.1. The strong correlation between magnitude and mass is expected as more massive galaxies tend to be more luminous. In addition, both are calculated here from the fit performed by the `kcorrect` tool (Blanton & Roweis 2007). There is a population of objects that define a "second" locus or whose M_i or mass determinations are flawed. We differentiate these objects by eye (dashed line) and consider the possibility that these contain a central AGN that dominates the host galaxy SED (see Section 5.5).

2007), so subtraction of a canonical normalized SED could introduce other errors. (2) Where spectra are available, the AGN contribution can be estimated and removed from the host galaxy SED. With limited spectroscopic coverage (∼2.5% of our galaxies have spectra), this too is an imperfect approach for these data. (3) Lastly, fitting of high-quality imaging data can successfully deconvolve the AGN point source from the host galaxy light. However, since the large majority of our objects are faint such an approach is not feasible.

We instead make a qualitative assessment of how an AGN contribution to our host galaxy SED would bias our fractions. In Figure 14, we plot the i-band absolute magnitude versus the stellar mass of our galaxy sample (small points) and the X-ray-detected subset (stars), color-coded according to the following $(u - r)_0$ color sequences: blue: $(u - r)_0 \leqslant 1.8$, green: $1.8 < (u - r)_0 < 2.6$, and red: $(u - r)_0 \geqslant 2.6$. Since more massive galaxies tend to be more luminous, it is not remarkable that these quantities show a strong correlation. In our analysis, the galaxy magnitudes and masses are derived using the same fit to the models implemented in the Blanton & Roweis (2007) `kcorrect` tool, further insuring a correlation between the two. We note a distinct second population of blue objects with apparently higher masses and brighter luminosities; we demarcate this "second sequence" by eye (as indicated by the black dashed line in Figure 14). Using this simple cut, we identify 3023 X-ray-observed and 156 X-ray-detected galaxies where AGN contamination may be an issue. These objects are indicated in Figures 6 and 14 (black points (observed) and black open circles (detected)). Where we have only upper limits to the X-ray luminosity, the galaxies' very blue colors are our primary evidence that they host an AGN. To be conservative, here we assume that all of these galaxies do host an AGN whose X-ray emission is either weak or obscured, but whose optical continuum substantially contaminates the colors.

We might explain this second sequence by speculating that the k-correction and derived M_i and stellar mass for these objects is incorrect. For example, we might estimate, based on Figure 5, that the derived M_i for these objects is too faint by about 1 mag. Hence, for an object at $M_i \sim -23$, we would correct up by 1 mag to $M_i \sim -24$. An object on the primary sequence at this magnitude corresponds to a stellar mass of log $M_{\rm star} \sim 11.8$, very reasonable for an AGN host.

Mischaracterization of the k-correction is also likely to bias our AGN fraction as a function of color, yielding an artificially high fraction in the blue sequence. We have, however, tested the impact of these "second sequence" objects on our global AGN fraction as a function of M_i and *bestz* and found that the fraction is robust to their inclusion (or exclusion).

Among these potentially contaminated objects, we associate 121 (4%) with QSO photometric redshifts—this compares to ∼0.3% of objects with QSO photometric redshifts in the Full sample. Another 83 have spectra, of which 66 have secure spectroscopic types: there are 50 broad-line AGNs (BLAGNs) identified via ChaMP spectroscopic follow-up, a single ChaMP NELG, and 15 SDSS MPA/JHU NELGs. Thus, a significant fraction of the objects along this second locus are indeed associated with active, star-forming galaxies and/or likely AGNs. However, since these objects lie preferentially outside of the limits of our five volume-limited samples—only one X-ray-detection and fewer than 300 galaxies across all five samples appear in our AGN fraction calculations—we do not recalculate $F_{\rm AGN}$ without these objects. We do, however, caution that AGN activity may bias our derived host galaxy properties in a small number of cases and in the highest-redshift, highest absolute magnitude sample, in particular.

White dwarfs are another possible contaminant in our galaxy sample. Their blue colors and X-ray brightness can cause them to masquerade as AGN, particularly if they have been incorrectly assigned a cosmological photometric redshift. However, since we removed objects with significant proper motions, we anticipate that these will not contribute more than an object or two to our numerator and thus will not seriously bias our fractions.

6. DISCUSSION

In this section, we compare our results with previous AGN fraction measurements in the field and in groups/clusters. We also expand our analysis of the AGN fraction as a function of host galaxy properties. To extract Vega UBVRI absolute magnitudes, k-corrections, and masses, we re-run the `kcorrect` tool on our Full galaxy sample (Bessell 1990; Blanton & Roweis 2007); these photometric bands are useful for comparisons with other studies in the literature.

6.1. Comparison to Previous Field Fractions

Page (2001) combines the present-day optical luminosity function of galaxies with the X-ray luminosity function of Seyfert 1s to calculate an expected AGN fraction. To reproduce the local type 1 AGN X-ray luminosity function for a plausible mix of AGN hosts, including both early- and late-type galaxies, he finds a Seyfert 1 fraction of about 1% at $z \sim 0$. This compares favorably to our direct measurement using intermediate-luminosity galaxy sample 3 ($-21 > M_i > -22$) at low redshift, for which we find an AGN fraction of $1.27\% \pm 0.18\%$.

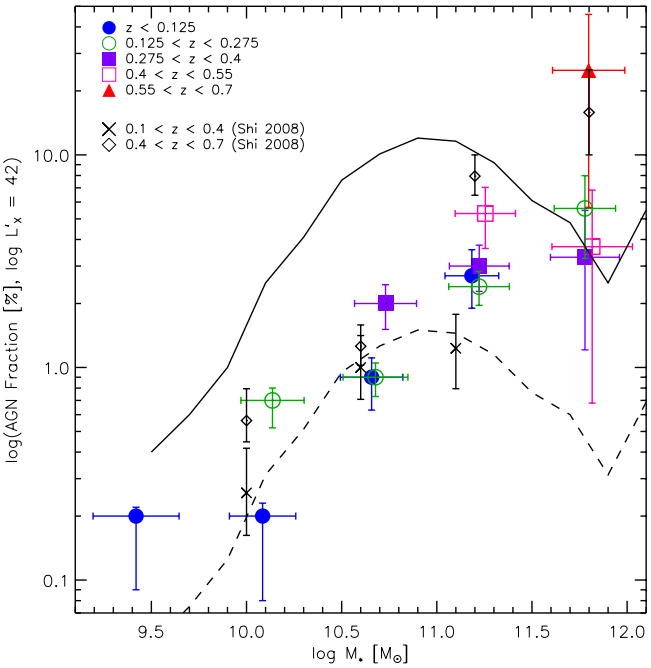

Figure 15. log of the AGN fraction (log $L'_X = 42$; solid black line in the right panel of Figure 6) vs. stellar mass. Colored symbols indicate our AGN fractions for five redshift intervals ($z < 0.125$, blue filled circles; $0.125 < z < 0.275$, green open circles; $0.275 < z < 0.4$, purple filled squares; $0.4 < z < 0.55$, magenta open squares; $0.55 < z < 0.7$, red filled triangles) from the mass-selected samples of Figure 9 (left panel). The high- and low-redshift fractions from Shi et al. (2008) are plotted as black symbols ($0.1 < z < 0.4$ as crosses, $0.4 < z < 0.7$ as open diamonds). The solid line shows the trend of the SDSS powerful AGN fraction with the host stellar mass from Kauffmann et al. (2003); the dashed line shows the same trend with the normalization decreased by a factor of eight (following Shi et al. 2008).

(A color version of this figure is available in the online journal.)

From a compilation of deep X-ray surveys (including the *Chandra* Deep Fields, the *Chandra* Large-Area Synoptic X-Ray Survey of Lockman Hole (CLASXS), and the All-wavelength Extended Groth strip International Survey (AEGIS); covering ~ 2 deg^2), Shi et al. (2008) derive an X-ray AGN fraction as a function of host stellar mass. We present the AGN fraction versus host mass in Figure 15 for our ChaMP/SDSS sample (colored symbols indicate our five redshift intervals) and from Shi et al. (2008) (black symbols; crosses for $0.1 < z < 0.4$ and diamonds for $0.4 < z < 0.7$). The fractions from these studies agree to within 1σ in all but one case, the highest mass bin of their low-redshift sample, where the agreement is good to within 1.5σ. We also include a comparison to the powerful AGN fraction from an optical, spectroscopic study of SDSS galaxies (solid black line; Kauffmann et al. 2003). Shi et al. (2008) re-normalize this relation by a factor of eight to fit their data and account for differences between the X-ray and optical selection functions, e.g., emission-line-selected AGN samples are more complete (less sensitive to obscuration) for low-mass galaxies at low redshift than X-ray-selected AGNs (Heckman et al. 2005). The Kauffmann et al. (2003) SDSS powerful AGN fraction is measured for $z < 0.3$ and shows an increase with stellar mass to $10^{11}\ M_\odot$ and then a sharp decrease toward galaxies of higher masses. Shi et al. (2008) interpret their low-redshift sample as demonstrating a turnover (or flattening) in the AGN fraction near $10^{11}\ M_\odot$, though no such inflection is detected for their high-redshift sample. Neither our low- or high-redshift samples show a turnover in the fraction, but instead increase from the lowest-mass to the most massive galaxies in our study.

We also compare our field AGN fraction to the zCOSMOS survey results (Silverman et al. 2009a), which utilize *XMM-Newton* observations of the COSMOS fields. For a mass limit of $\log M_\star > 10.4$ (black dashed line in the right panel of Figure 9), we match the redshift and X-ray luminosity intervals used by Silverman et al. (2009a) in their Figure 11: $0.1 < z < 0.58$ and $0.58 < z < 1.05$, with $L_X > 10^{42.5}$ erg s^{-1} (dashed black line in the right panel of Figure 9). In the low-redshift bin, we have 186 X-ray detections and 19,057 X-ray-observed galaxies; these yield an AGN fraction of $0.98\% \pm 0.07\%$. The zCOSMOS field fraction in this bin is $1.9\% \pm 0.6\%$. Hence, our field AGN fraction falls below the zCOSMOS field fraction by 1.5σ. The difference between the ChaMP/SDSS and zCOSMOS low-redshift results may reflect evolution in the AGN fraction if the zCOSMOS sample is weighted toward higher-redshift objects (in the low-redshift bin the ChaMP/SDSS sample has an average redshift of $\langle z \rangle = 0.28$). In the high-redshift bin, we find 14 detections and 296 limits, which yield a fraction of $5.03\% \pm 1.25\%$, versus the zCOSMOS value of $3.7 \pm {}^{0.6}_{0.5}\%$. However, we do not consider this second a robust comparison because our sample is not complete beyond redshifts of 0.4 for this mass cut (see Figure 9, left panel).

Evidence for evolution in the AGN fraction has been seen in other recent work. Lehmer et al. (2007) use the *Chandra* Deep Fields to study the AGN fraction in early-type galaxies (to $z \sim 0.7$) and find evolution consistent with the $(1+z)^3$ PLE model frequently fit to the luminosity function of X-ray-selected AGNs (hereafter, the AGN XLF; Ueda et al. 2003; Barger et al. 2005; Hasinger et al. 2005). Similar behavior is also noted in an earlier analysis of the stacked X-ray properties of early-type galaxies in a 1.4 deg^2 field in the NOAO Deep Wide-Field Survey (Brand et al. 2005). (Note, however, in a study of late-type galaxies, Lehmer et al. (2008) find no evidence for evolution of the AGN fraction over the redshift range $0.1 < z < 0.8$.) In the left panel of Figure 13, we show curves for PLE ($\propto (1+z)^3$; gray dotted line) and for LDDE, another popular model for the evolution of the AGN XLF ($\propto (1+z)^4$; gray dashed line). These curves are intended to be illustrative only and are thus arbitrarily normalized to the mean AGN fraction in the four M_i bins with $0.125 \leqslant z < 0.275$. For the $-22.0 \geqslant M_i > -23.0$ magnitude bin, we compare the AGN fraction in the lowest- and highest-redshift intervals and find, $F_{\rm AGN}(z = 0.47) = 2.2 \pm {}^{+2.5}_{-1.1} \times F_{\rm AGN}(z = 0.09)$; i.e., though poorly constrained, the change in this AGN fraction is consistent with either $(1+z)^3$ or $(1+z)^4$ evolution.

In the current work, we predicate our comparison to the AGN XLF on the assumption that the underlying galaxy population does not evolve substantially between redshifts of $z = 0.5$ and the present day—indeed, we assume no evolution in our galaxy k-corrections. Thus, the evolution of the AGN fraction is entirely attributed to the evolution of the X-ray-detected AGN population. The assumption of zero evolution for the galaxy population is almost certainly too simple, particularly for late-type galaxies, which have been shown to fade by a magnitude or more between $z \sim 1$ and the present (Lilly et al. 1995; Wolf et al. 2003; Faber et al. 2007). In fact, the lack of evolution of the AGN fraction in late types reported by Lehmer et al. (2008), may indicate that the AGN and late-type galaxy populations co-evolve for $z < 1$.

6.2. Comparison to Cluster and Group X-ray Fractions

The impact of environment on the formation and evolution of accreting SMBHs remains an important open question, i.e., are

Table 4
Comparison to Cluster Fractions

$M_R <$	log L_X		N_{det}	N_{lim}	F_{field}[a] (%)			F_{clust}[b] (%)
	Min	Max			Min	Mean	Max	
−20	40.9	43.6	26	448	4.89	6.00	7.11	6.0
−20	41.0	...	28	642	3.69	4.50	5.31	4.9
−20	42.0	...	113	9588	1.08	1.19	1.30	1.0
−21.3	41.0	...	25	208	10.12	12.38	14.64	9.8
−21.3	41.0	...	4	46	6.14	10.42	14.71	5.5

Notes.
[a] The field fractions calculated from the ChaMP and SDSS survey data and described in the present work for $0.05 < z < 0.31$.
[b] The first four cluster fractions come from Martini et al. (2007) and also span $0.05 < z < 0.31$; the final comparison is to Sun et al. (2007) clusters with $0.01 < z < 0.05$. Absolute R magnitudes are calculated via the SDSS transformations described in Section 4.1. The Sun et al. (2007) result in the table is a simple fraction determined from their values of 9 AGNs and 163 galaxies. The mean AGN fraction for these inputs, calculated via the beta distribution, is 6.1%.

AGN preferentially located in field galaxies, in galaxy groups, or in rich clusters? Early studies revealed a paucity of optically luminous AGNs in clusters (Dressler et al. 1985), compared to the field—7% versus 31% of galaxies had emission-line nuclei in clusters versus the field, and 1% versus 5% harbored AGNs. Giovanelli & Haynes (1985) proposed that galaxies in clusters lose cold gas from their disks by interacting with the cluster core, leaving behind a cluster galaxy population deficient in the cold gas necessary to fuel AGN. A smaller frequency of AGN fueling events was also proposed—in this scenario, the merger of two gas-rich galaxies was invoked as the mechanism for driving cold inflows toward a massive central black hole (Barnes & Hernquist 1992). If galaxies in the cluster environment experience fewer mergers due to their high velocity dispersions, less AGN activity would result. These two scenarios might also work in tandem to produce smaller AGN fractions in clusters. (Note that groups, which have lower velocity dispersions than clusters, should have merger rates closer to those in the field.)

The last decade has shown great advances in our understanding of the X-ray-selected population of AGNs in clusters of galaxies (Martini et al. 2002, 2006, 2007, 2009). Enabled by the exceptionally high sensitivity and spatial resolution of *Chandra*, Martini et al. (2002) and Martini et al. (2007) showed that the fraction of X-ray-selected AGN observable in clusters at $0.05 < z < 0.31$ was, in fact, higher than previously reported and similar to the field, though the field fraction has historically been poorly constrained.

To compare our robust field X-ray AGN fractions to those reported for clusters, we employ absolute R magnitudes, M_R, adopt a variety of L'_X and M_R limits, and measure the active fraction for $0.05 < z < 0.31$ (to match the cluster redshift range of Martini et al. 2007). These comparisons are summarized in Table 4. Our field fractions for $M_R < -20$ are (1) $6.00\% \pm 1.11\%$ ($8 \times 10^{40}\,\mathrm{erg\,s^{-1}} < L_X < 4 \times 10^{43}$ erg s^{-1}), (2) $4.50\% \pm 0.81\%$ for a limiting $L_X = 10^{41}$ erg s^{-1}, and (3) $1.19\% \pm 0.11\%$ for a limiting $L_X = 10^{42}\,\mathrm{erg\,s^{-1}}$. These compare to cluster active fractions of 6.0%, 4.9%, and 1.0%, respectively. This excellent agreement between the field and cluster fractions is also borne out for a brighter magnitude cut. For $M_R < -21.3$ and a limiting $L_X = 10^{41}$ erg s^{-1}, we find a fraction of $12.38\% \pm 2.26\%$, which agrees with the Martini et al. (2007) value of 9.8% within 1.5σ. For these same magnitude and X-ray luminosity limits, we also find a fraction of $10.42\% \pm 4.29\%$ in the narrower redshift range ($0.01 < z < 0.05$) used by Sun et al. (2007), who find a cluster AGN fraction of 5.5%. The striking concordance between cluster and field fractions out to $z \sim 0.3$ implies that AGN activity at low redshift does not depend strongly on local density.

There are various scenarios for why the field and cluster fractions might be the same. As described in Martini et al. (2009), it is possible that blue, late-type galaxies in clusters are still in-falling and have not yet been stripped of their gas by interactions with the cluster potential. As a result, these galaxies might retain enough cold gas to fuel an AGN, as is the case in the field. In another scenario, red, early-type galaxies may keep their cold gas (despite interactions with cluster potential) and thus continue to host an active SMBH. A third possibility invokes evolution of the AGN fraction in both clusters and in the field—here, AGN activity was more dependent on environment in the past, e.g., closer to the peak in the AGN number density at $z \sim 2$, but at the present-day galaxies in both environments are relatively quiescent and the differences between the field and clusters is not discernible. This last scenario can be tested by probing the AGN fraction in both clusters and the field at high redshifts (and possibly in regimes where low-luminosity AGN dominate).

As discussed in Sections 5.3 and 6.1, there is some evidence that the AGN fraction evolves as a function of redshift. Though we find the AGN fraction in clusters and in the field in close agreement at low redshift, they may begin to differ as we probe to higher-redshift regimes. Employing a method similar to Page (2001), Martini et al. (2009) estimate the field AGN fraction based on galaxy luminosity functions and compare it to their *Chandra* cluster fraction (see their Figure 3). At $z \sim 0.15$, they find the two in agreement, but at $z \sim 0.8$ the field fraction is nearly a factor of five higher than the cluster fraction. This gives some credence to a scenario wherein the cluster and field AGN fractions were more disparate at earlier times.

Other authors (Georgakakis et al. 2008a; Silverman et al. 2009a) have investigated the AGN fraction in groups of galaxies (or as a function of local overdensities). Using DEEP2 *Chandra* observations from AEGIS for $0.7 < z < 0.9$ and $M_B < -20$, Georgakakis et al. (2008a) find group and field fractions of $4.7\% \pm 1.6\%$ and $4.5\% \pm 1.0\%$, respectively. This group fraction is about five times higher than that reported by Martini et al. (2009) in clusters at similar redshifts. This discrepancy

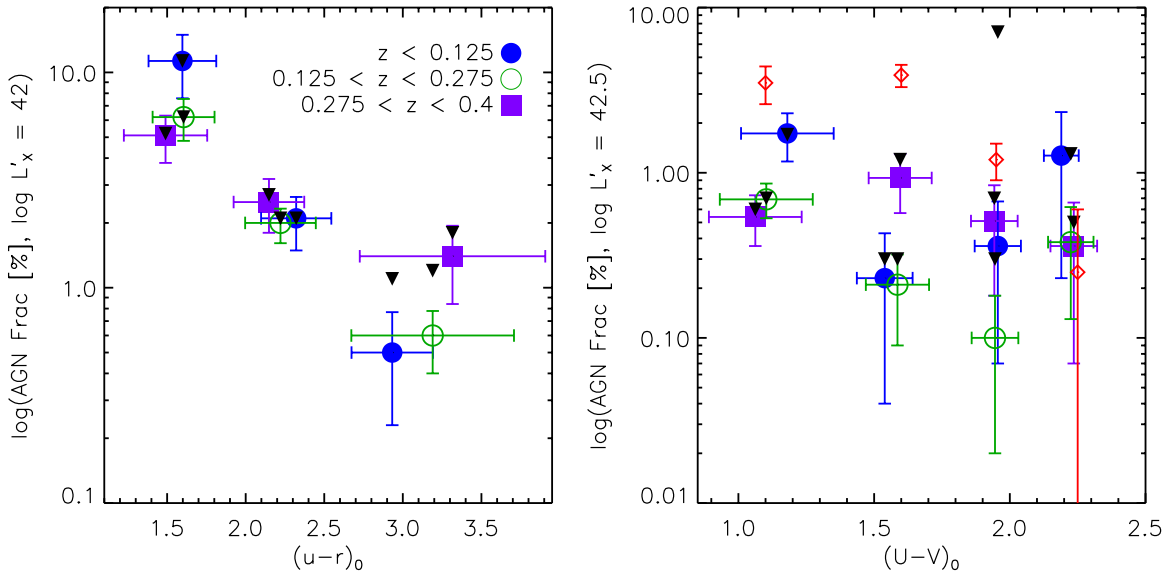

Figure 16. Left: the AGN fraction (log $L'_X = 42$, solid black line in the right panel of Figure 6) for three low-redshift samples, binned also by $(u-r)_0$ color (see Section 6 for discussion). Right: similar to the left panel, but the data are binned instead by $(U-V)_0$ color and the X-ray luminosity limit is fixed at log $L'_X = 42.5$ and plotted on a log scale (black dashed line in the right panel of Figure 6) to compare to zCOSMOS results (open red diamonds). Upper limits on the fractions are plotted as solid, downward-facing black triangles in both panels (see Section 5.5). The trend toward lower AGN fractions at redder colors is clearly visible for both color regimes.

(A color version of this figure is available in the online journal.)

may arise from intrinsic differences in the group and cluster environments at redshifts near $z \sim 1$, but more likely it originates from differences in the X-ray and optical selection criteria of the surveys; i.e., Georgakakis et al. (2008a) include lower-X-ray luminosity sources than do Martini et al. (2009) and their host galaxy magnitude limits differ. Using only the AEGIS data, Georgakakis et al. (2008a) report a higher AGN fraction in groups than in the field at $z \sim 1$, but attribute this to their finding that AGNs are preferentially found in red, luminous galaxies, which are themselves more likely to reside in higher density environments. They note that an exception to this trend may exist for the most X-ray-luminous AGNs, which appear in higher numbers in the field.

Silverman et al. (2009a) also study the X-ray AGN fraction for low-mass host galaxies ($10.4 < \log M_\star < 11$) in the field and in groups, and find no statistical difference between the fractions in these environments. They do report a trend for $\log M_\star > 11$, wherein high-X-ray luminosity AGNs are less common in more dense environs, see also Kauffmann et al. (2004) and Constantin et al. (2008). For $0.58 < z < 1.05$ and $\log M_\star > 10.4$, Silverman et al. (2009a) find a field fraction of $\sim 3.7\% \pm 0.5\%$ and a group fraction of $\sim 4\% \pm 1.2\%$, consistent with the findings of Georgakakis et al. (2008a).

We look to our highest-redshift bins to compare our field X-ray AGN fractions to those of Georgakakis et al. (2008a) and Silverman et al. (2009a). For $0.55 \leqslant z < 0.7$, our only complete mass bin is $11.6 \leqslant \log M_\star < 13$, for which we calculate an upper limit on the AGN fraction of $25.00\% \pm 20.80\%$. Note, however, that we base this estimate of the fraction on only two X-ray-observed host galaxies and zero X-ray detections and thus do not offer a sensitive probe of the field fraction (particularly within this redshift range). For $0.4 \leqslant z < 0.55$, we have two complete mass bins, $11 \leqslant \log M_\star < 11.6$ and $11.6 \leqslant \log M_\star < 13$, in which we measure AGN fractions of $5.33\% \pm 1.70\%$ and $3.70\% \pm 3.13\%$. Though these fractions are broadly consistent with the AEGIS and zCOSMOS studies, they sample higher-mass hosts at lower redshifts—our median redshifts are $\langle z \rangle = 0.44$ and $\langle z \rangle = 0.45$ for the low- and high-mass bins, respectively. To include lower-mass hosts (e.g., log $M_\star > 10.4$), we must set our redshift limit to $z = 0.4$ to achieve a complete sample, and questions about evolution begin to impede comparisons with the deep-field results.

We point out these higher-redshift results to illustrate that small number statistics continue to stymie measurements of the X-ray AGN fraction in all environments (field, group, and cluster), particularly at the faint end of the galaxy population and at high redshift.

6.3. AGN Host Galaxy Properties

To investigate the properties of our host galaxies, we show the AGN fraction in bins of *bestz* versus rest-frame $(u-r)_0$ and $(U-V)_0$ color (Figure 16, left and right panels, respectively). The $(u-r)_0$ blue, green, and red color bins are $(u-r)_0 \leqslant 1.8$, $1.8 < (u-r)_0 < 2.6$, and $(u-r)_0 \geqslant 2.6$. The green bin straddles the $(u-r)_0 = 2.2$ divide between blue and red galaxies defined by Strateva et al. (2001). The $(U-V)_0$ color bins are $0.8 < (U-V)_0 < 1.4$, $1.4 < (U-V)_0 < 1.8$, $1.8 < (U-V)_0 < 2.1$, and $2.1 < (U-V)_0 < 2.4$, selected to match the zCOSMOS color bins (Silverman et al. 2009b, their Figure 12(b)). We apply a mass cut of $\log M_\star > 10.6$ (black solid line in the right panel of Figure 9), again to match the zCOSMOS study of host galaxy colors, and include only the redshift ranges associated with our samples 1*–3*, as these are complete for this mass cut. For the $(u-r)_0$ comparison we employ the X-ray limit used throughout this work ($L_X = 10^{42}$ erg s^{-1}); for the zCOSMOS $(U-V)_0$ comparison we use $L_X = 10^{42.5}$ erg s^{-1} as in Silverman et al. (2009b).

In the $(u-r)_0$ bins, the fraction of AGN in the blue sequence is larger than that in either the red sequence or the green valley, for all three redshift intervals (Figure 16, left panel, colored symbols). This trend toward a larger AGN fraction in

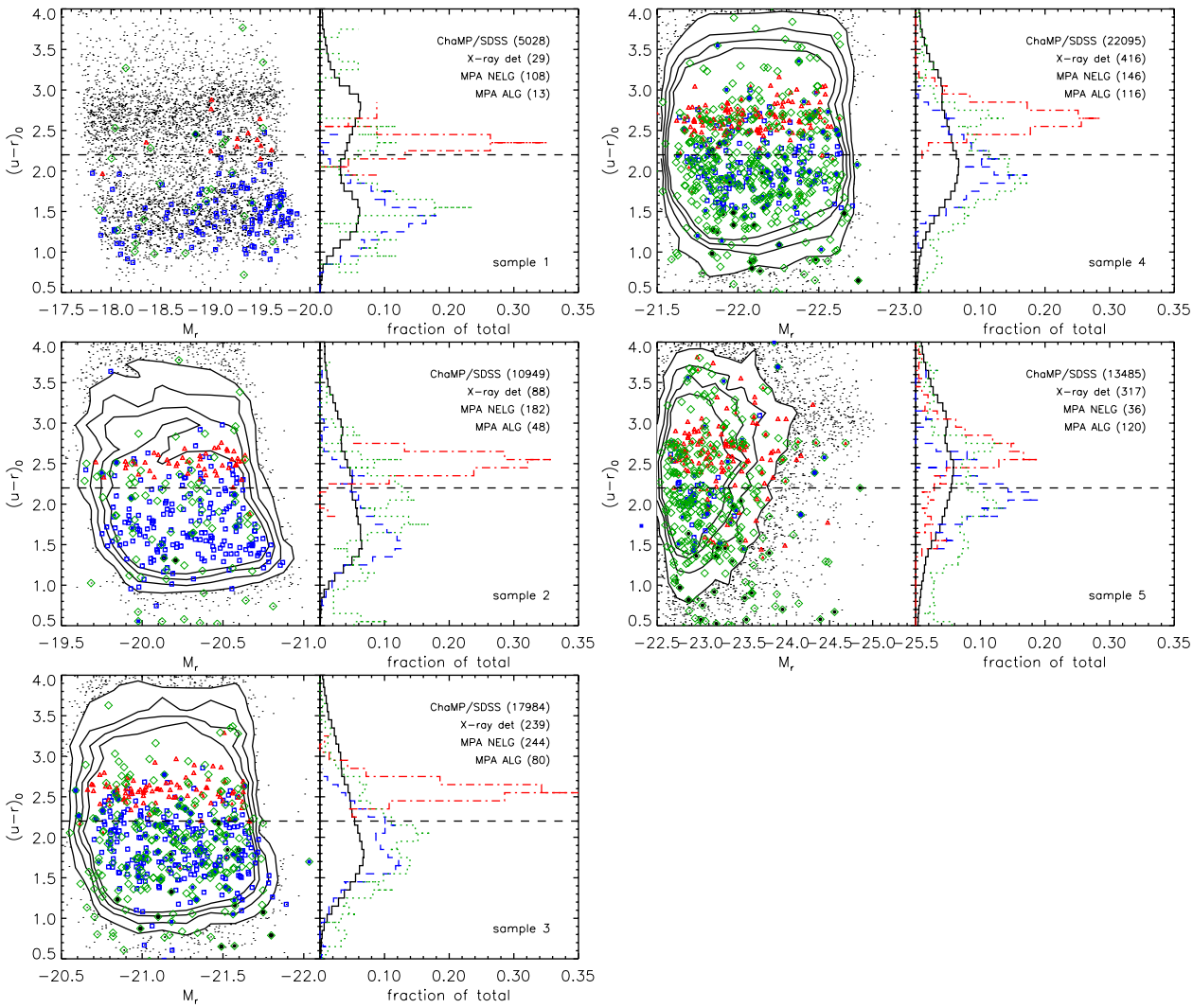

Figure 17. Left sub-panels: rest-frame $(u - r)$ as a function of r-band absolute magnitude for the Full galaxy sample (black dots), the X-ray-detected sample (open green diamonds), and objects with spectra: ChaMP/SDSS NELG (open blue squares), ChaMP/SDSS X-ray-detected NELG (filled blue squares), ChaMP/SDSS ALG (open red triangles), ChaMP/SDSS X-ray-detected ALG (filled red triangles), SDSS BLAGN (open black circles), and ChaMP BLAGN (filled black circles). Right sub-panels: histogram of $(u - r_0)$ for the Full photometric sample (black solid line), the X-ray-detected sample (green dotted line), the SDSS spectroscopic NELG sample (dashed blue line), and the SDSS spectroscopic ALG sample (dot-dashed red line). The $(u - r)_0 = 2.2$ division between the red and blue sequences from Strateva et al. (2001) is shown in both panels (dashed black line).

(A color version of this figure is available in the online journal.)

the blue sequence persists when the red point sources, which might bias the red sequence and/or the green valley toward a lower AGN fraction, are removed (Figure 5, green points; see also Section 5.5). "Upper limit" AGN fractions, calculated without these red point sources, are shown in Figures 13 and 16 (filled, black, downward-facing triangles). This result is in contrast to multiple studies, which have found that AGNs lie preferentially in the valley between the red and blue galaxy sequences, e.g., Georgakakis et al. (2008a), Georgakakis et al. (2008b), Silverman et al. (2008), and Schawinski et al. (2010); though Silverman et al. (2008) associate the green valley peak with large-scale structures at particular redshifts. Our finding agrees, however, with more recent studies of the zCOSMOS fields (Silverman et al. 2009a, 2009b); these authors argue that the peak reported in the transition region between blue and red galaxies is an artifact that can be eliminated by applying an appropriate mass cut, as we have done here.

As discussed in Section 5.5, the AGN central engine may contribute considerable light to the SDSS SED, making the object appear artificially blue. AGN contamination of the host galaxy light would result in an overestimate of the number of galaxies along the blue sequence. We do not expect this effect to be large, however, since the majority of the X-ray sources in our three lowest-redshift bins ($z \leqslant 0.4$) have $L_X < 10^{44}$ erg s^{-1} (Figure 6, left panel); hence, accretion onto the central SMBH is probably not powerful enough to significantly contaminate the host galaxy light (Prieto et al. 2010). A population of starburst galaxies, whose X-ray luminosities can be as high as $L_X \sim 10^{42}$ erg s^{-1}, might also contaminate our blue sequence, but such X-ray-bright star-forming galaxies are more likely at higher redshift ($z > 0.4$; Yan et al. 2010).

To further explore the properties of our sample as a function of host galaxy properties, we compare our primarily photometric Full galaxy sample to our spectroscopic sub-sample. Figure 17 shows $(u - r)_0$ color versus absolute r-band magnitude (M_r; left panels), and $(u - r)_0$ color histograms (right panels) for each of our five volume-limited samples. In the left-hand panels, we overplot spectroscopic types for all galaxies that have secure

line identifications in the MPA/JHU DR7 catalog, as well as those identified via ChaMP spectroscopic follow-up (filled symbols indicate X-ray detections, open symbols mark X-ray non-detections): blue squares are NELGs; red triangles show ALGs; black circles mark BLAGN. We also indicate X-ray-detected sources, with and without spectroscopic classifications, as open green diamonds. In the right-hand panels, we show $(u - r)_0$ histograms for the Full galaxy sample (solid black line), the X-ray-detected sub-sample (green dotted line), as well as for the MPA/JHU NELG (blue dashed line) and ALG (red dot-dashed line) samples. The histograms are each normalized to the total number of objects within the (sub-)sample, shown in parentheses in the relevant figure.

We see a clear division between the NELG and ALG samples in Figure 17, with NELGs falling along the blue sequence and ALGs along the red sequence. We do not see an overdensity of X-ray sources in the green valley between the red and blue sequences, as has sometimes been reported elsewhere (Georgakakis et al. 2008a, 2008b; Silverman et al. 2008; Schawinski et al. 2010). In the color histograms, the Full galaxy sample demonstrates a clear bi-modality at low redshift, but this trend becomes washed out (or perhaps shifted) at higher redshift. This may result from evolution in the galaxy population, from smearing due to photo-z uncertainties, or from stellar interlopers. As an illustration of this last possibility, we note that for sample 1 (Figure 17, first panel) the peak of the red sequence in the Full galaxy sample (solid black line) is redder than the spectroscopic ALG sample (red dot-dashed line)—this offset may be due to a population of M-dwarf stellar contaminants amongst the objects with photometric redshifts. Here again, contamination of the host color by a luminous central engine may force galaxies out of the green or red portions of the diagram and onto the blue sequence (see Section 5.5), blurring the expected bi-modality in the underlying galaxy population. However, since such contamination is unlikely in the majority of the non-X-ray-detected (Full galaxy) sample, we do not expect the effect to be large enough to explain the trends we see here.

We also compare the $(U - V)_0$ results (Figure 16, right panel) to the field fraction determined in the 10k catalog of the zCOSMOS spectroscopic redshift survey (Silverman et al. 2009a, 2009b). The Silverman et al. (2009b) fractions for these four $(U - V)_0$ bins (estimated from their Figure 12(b)) are approximately $3.5\% \pm 0.9\%$, $3.9\% \pm 0.6\%$, $1.2\% \pm 0.3\%$, and $0.25\% \pm 0.35\%$ (Figure 16, right panel, red open diamonds). We compare these to our $(U - V)_0$ fractions (taking a weighted averaged over our three redshift bins) of $0.67\% \pm 0.12\%$, $0.26\% \pm 0.10\%$, $0.14\% \pm 0.08\%$, and $0.40\% \pm 0.19\%$. As was the case for the global field fraction (Section 6.1), our ChaMP/SDSS fractions fall significantly lower than the zCOSMOS fractions, except in the reddest color bin. The zCOSMOS sample is almost certainly weighted toward higher redshifts (their redshift range is $0.1 < z < 1.02$, versus ours for this comparison, $0.0025 < z < 0.4$). Thus, we might rather compare only to our AGN fraction in the highest-redshift bin ($0.275 < z < 0.4$), i.e., $0.54\% \pm 0.19\%$, $0.93\% \pm 0.37\%$, $0.51\% \pm 0.33\%$, and $0.36\% \pm 0.3\%$. Even here, our field AGN fractions are systematically lower than those found in the zCOSMOS survey; they disagree by approximately 3σ in the blue and green sequences, by roughly 2σ in the red sequence, and agree within the errors only in the reddest color bin. Despite these differences, both our AGN fractions and the zCOSMOS fractions are largest for host galaxies with blue colors. Silverman et al. (2009b) propose that this trend might establish a connection between accretion onto SMBH and star formation out to $z \sim 1$. Our findings lend additional support to this hypothesis.

It is plausible that the difference between the field AGN fractions from ChaMP/SDSS and zCOSMOS arises from evolution in the AGN fraction. If we assume a mean redshift for the zCOSMOS sample of $z \sim 0.6$, and a mean redshift of $z \sim 0.3$ for our sample 3, we would expect PLE $(1 + z)^3$ evolution in the AGN XLF to yield a zCOSMOS fraction that is a factor of $\sim$2 higher than the ChaMP/SDSS fraction. Such a correction would bring our results closer to the zCOSMOS blue and green sequence fractions, and achieve agreement in the red sequence. Note that the fractions in the reddest bin would, however, begin to disagree. Evolution of the underlying host galaxies colors may explain these differences, e.g., AGN activity might occur most often in blue galaxies at higher redshifts ($z > 0.5$), but increasingly shift toward red galaxies in the local universe (see also discussions in Silverman et al. 2008, 2009b).

7. CONCLUSIONS

We present a study of the X-ray-active fraction of field galaxies in an extensive catalog of more than 100,000 galaxies with X-ray and optical coverage from *Chandra* and SDSS ($\sim$1600 are X-ray detected). We combine ChaMP/SDSS spectroscopic and photometric redshifts with X-ray and optical fluxes (or flux limits) to assign absolute magnitudes, X-ray luminosities (or limits), masses, and colors to each galaxy in the sample. With these data we explore the AGN fraction (L_X(0.5–8 keV) $> 10^{42}$ erg s^{-1}) in five independent samples, complete in redshift and i-band absolute magnitude:

1. $F_{\mathrm{AGN},1} = 0.16\% \pm 0.06\%$ ($z \leqslant 0.125$, $-18 > M_i > -20$),
2. $F_{\mathrm{AGN},2} = 0.50\% \pm 0.11\%$ ($z \leqslant 0.275$, $-20 > M_i > -21$),
3. $F_{\mathrm{AGN},3} = 1.27\% \pm 0.18\%$ ($z \leqslant 0.400$, $-21 > M_i > -22$),
4. $F_{\mathrm{AGN},4} = 2.85\% \pm 0.39\%$ ($z \leqslant 0.550$, $-22 > M_i > -23$),
5. $F_{\mathrm{AGN},5} = 3.80\% \pm 0.92\%$ ($z \leqslant 0.700$, $M_i < -23$).

The low-redshift bin edge for these fractions is $z = 0.0025$, selected to avoid galactic objects and photometric redshift artifacts.

Our robust analysis is enabled by ChaMP's comprehensive sensitivity maps for ACIS imaging, which allow recognition of imaged-but-undetected objects, counts limits for 50% and 90% detection completeness, and corresponding flux upper limits at any sky position. The AGN (or X-ray-active) fraction for each volume-limited sample, as well as the asymmetric error bars, are calculated via the β distribution—an ideal statistical tool for evaluating fractions, particularly when the numerator and denominator are not drawn from independent samples.

We find excellent agreement between our ChaMP/SDSS field AGN fraction and the *Chandra* cluster AGN fraction, for samples restricted to similar redshift and absolute magnitude ranges. For ChaMP/SDSS field galaxies with $0.05 < z < 0.31$ and absolute R-band magnitude more luminous than -20, $F_{\mathrm{AGN}} = 1.19\% \pm 0.11\%$. The Martini et al. (2007) X-ray cluster fraction for this redshift and M_R is 1.0%. We find good agreement between our field fraction and the cluster fraction for a variety of other absolute R-band magnitude and X-ray luminosity limits as well. Our results are also broadly consistent with measures of the field AGN fraction in narrow, deep fields, though differences in the optical selection criteria, redshift coverage, and possible cosmic variance between fields introduce larger uncertainties in these comparisons.

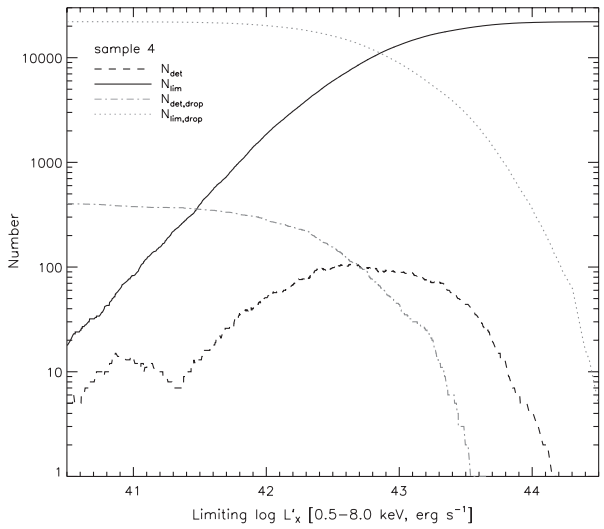

Figure 18. Numbers of X-ray-detected ($N_{\rm det}$) and X-ray-observed ($N_{\rm lim}$) galaxies included in the X-ray-active fraction at each X-ray threshold for sample 4 are shown as black dashed and solid lines, respectively. The numbers of objects that are "dropped" at each limit are also shown (gray dot-dashed line for X-ray-detections [$N_{\rm det,drop}$], gray dotted line for X-ray-observed objects [$N_{\rm lim,drop}$]). This plot makes explicit the shape of the X-ray-active fraction curve in Figure 10, i.e., while the number of X-ray-detections included in the sample ranges from a few to several tens of objects between log L_X of 40.5 and 44, the number of X-ray-observed galaxies increases from about 20 to more than 20,000 in the same range. In this optically complete sample, the majority of the brightest X-ray sources make it into the fraction, while many X-ray-low-luminosity sources are eliminated.

In our analysis of the AGN fraction, as well as in our comparison to deep-field studies, we find evidence that the AGN fraction evolves with redshift. Our data are consistent with either $(1 + z)^3$ or $(1 + z)^4$ evolution, i.e., the two most common fits to the X-ray AGN luminosity function, but likely also depend on evolution in the host galaxy population. These findings are tantalizing, but poorly constrained and require high-quality wide-field data at redshifts out to (and above) $z \sim 1$ for verification. We test the impact of host galaxy color (for stellar masses log $M_\star > 10.6$) and find that the AGN fraction is largest for hosts with blue colors, though this trend too may depend on redshift. Since galaxy and AGN evolution are both affected by environment, we are embarking on a clustering study of AGN activity versus environment to quantify these properties. A comparison between cluster, group, and field fractions at redshifts approaching $z = 2$ would be particularly compelling.

We thank the referee for comments that improved this manuscript, Nicolas B. Cowan for useful discussions about the β distribution and Monte Carlo simulations, Adam D. Myers for providing QSO redshift probability distributions for the MC simulations, and John D. Silverman for assistance with the comparisons to the zCOSMOS AGN fractions. Support for this work was provided by the National Aeronautics and Space Administration through Chandra Award Number AR7-8015A-R0, AR9-0020X, and GO0-11129B issued by the Chandra X-ray Observatory Center, which is operated by the Smithsonian Astrophysical Observatory for and on behalf of the National Aeronautics Space Administration under contract NAS8-03060. This research was also supported in part by the National Science Foundation under grant No. NSF PHY05-51164. D.H. acknowledges support from the NASA Harriett G. Jenkins Predoctoral Fellowship Program and the University of Washington Astronomy Department's Jacobsen Fund. We acknowledge use of the NASA/IPAC Extragalactic Database (NED), operated by the Jet Propulsion Laboratory, California Institute of Technology, under contract with the National Aeronautics and Space Administration.

Funding for the SDSS and SDSS-II has been provided by the Alfred P. Sloan Foundation, the Participating Institutions, the National Science Foundation, the U.S. Department of Energy, the National Aeronautics and Space Administration, the Japanese Monbukagakusho, the Max Planck Society, and the Higher Education Funding Council for England. The SDSS Web site is http://www.sdss.org/. The SDSS is managed by the Astrophysical Research Consortium for the Participating Institutions. The Participating Institutions are the American Museum of Natural History, Astrophysical Institute Potsdam, University of Basel, Cambridge University, Case Western Reserve University, University of Chicago, Drexel University, Fermilab, the Institute for Advanced Study, the Japan Participation Group, Johns Hopkins University, the Joint Institute for Nuclear Astrophysics, the Kavli Institute for Particle Astrophysics and Cosmology, the Korean Scientist Group, the Chinese Academy of Sciences (LAMOST), Los Alamos National Laboratory, the Max Planck Institute for Astronomy (MPIA), the Max Planck Institute for Astrophysics (MPA), New Mexico State University, Ohio State University, University of Pittsburgh, University of Portsmouth, Princeton University, the United States Naval Observatory, and the University of Washington.

Facilities: CXO, Sloan, FLWO:1.5m (FAST spectrograph), Magellan:Baade (LDSS2 imaging spectrograph), Magellan:Clay (IMACS), WIYN (Hydra)

APPENDIX

In Section 5.1, we define the fraction of X-ray-active galaxies. We apply both optical and X-ray completeness criteria to insure an accurate measure of the fraction. In this Appendix, we describe the objects that appear in our volume-limited optical samples, but do not pass the X-ray cuts. These "dropped" objects can be described by

$$N_{\rm lim,drop} = \sum_{z_{\rm min}}^{z_{\rm max}} \sum_{M_{\rm faint}}^{M_{\rm bright}} \sum_{L'_X}^{\infty} G(L_{X,\rm lim}, M_i, bestz), \quad \text{(A1)}$$

$$N_{\rm det,drop} = \sum_{z_{\rm min}}^{z_{\rm max}} \sum_{M_{\rm faint}}^{M_{\rm bright}} \sum_{L'_X}^{\infty} \sum_{L'_X}^{\infty} X(L_X, L_{X,\rm lim}, M_i, bestz), \quad \text{(A2)}$$

where $N_{\rm lim,drop}$ quantifies the number of X-ray-observed objects "dropped" from the denominator, and $N_{\rm det,drop}$ describes the number of X-ray-detected sources eliminated from the numerator.

In Figure 18, we show the behavior of $N_{\rm det}$, $N_{\rm lim}$, $N_{\rm det,drop}$, and $N_{\rm lim,drop}$ as a function of limiting X-ray luminosity for sample 4. Comparing this to the top, right panel of Figure 10, it is clear that the high X-ray-active fraction below log $L'_X \sim 41.4$ can be explained by a relatively small number of both X-ray-detected and X-ray-observed galaxies. At higher limiting X-ray luminosities, the number of X-ray detections in the numerator increases (until log $L'_X \sim 43$), but the number of galaxies that might have been detected at this threshold X-ray luminosity (the denominator) increases even more rapidly, leading to an overall decline in the X-ray-active fraction. At the highest luminosities, the number of X-ray-detected sources falls off sharply while the number of X-ray-observed galaxies continues to climb; the

fraction drops to zero, accordingly. The error intervals shown in Figure 10 are intuitive insofar as they are largest where the number of objects used to determine the fraction is small, and smallest in the opposite extreme.

REFERENCES

Abazajian, K., et al. 2003, AJ, 126, 2081
Abazajian, K., et al. 2004, AJ, 128, 502
Abazajian, K., et al. 2005, AJ, 129, 1755
Abazajian, K. N., et al. 2009, ApJS, 182, 543
Adelman-McCarthy, J. K., et al. 2006, ApJS, 162, 38
Adelman-McCarthy, J. K., et al. 2008, ApJS, 175, 297
Adelman-McCarthy, J. K., et al. 2007, ApJS, 172, 634
Aldcroft, T. L., Green, P., Kashyap, V., Kim, D., & Connelly, J. 2008, High Energy Astrophysics Division Meeting, AAS Publications, 10, 04.02
Ball, N. M., Brunner, R. J., Myers, A. D., Strand, N. E., Alberts, S. L., & Tcheng, D. 2008, ApJ, 683, 12
Barger, A. J., Cowie, L. L., Mushotzky, R. F., Yang, Y., Wang, W., Steffen, A. T., & Capak, P. 2005, AJ, 129, 578
Barnes, J. E., & Hernquist, L. 1992, ARA&A, 30, 705
Bessell, M. S. 1990, PASP, 102, 1181
Best, P. N., Kauffmann, G., Heckman, T. M., Brinchmann, J., Charlot, S., Ivezić, Ž., & White, S. D. M. 2005, MNRAS, 362, 25
Blanton, M. R., & Roweis, S. 2007, AJ, 133, 734
Brandt, W. N., & Hasinger, G. 2005, ARA&A, 43, 827
Brand, K., et al. 2005, ApJ, 626, 723
Brinchmann, J., Charlot, S., Heckman, T. M., Kauffmann, G., Tremonti, C., & White, S. D. M. 2004, arXiv:astro-ph/0406220
Bruzual, G., & Charlot, S. 2003, MNRAS, 344, 1000
Budavári, T., et al. 2001, AJ, 122, 1163
Chabrier, G. 2003, PASP, 115, 763
Civano, F., et al. 2007, A&A, 476, 1223
Cocchia, F., et al. 2007, A&A, 466, 31
Constantin, A., Green, P., Aldcroft, T., Kim, D., Haggard, D., Barkhouse, W., & Anderson, S. F. 2009, ApJ, 705, 1336
Constantin, A., Hoyle, F., & Vogeley, M. S. 2008, ApJ, 673, 715
Covey, K. R., et al. 2007, AJ, 134, 2398
Covey, K. R., et al. 2008, ApJS, 178, 339
Cowie, L. L., Songaila, A., Hu, E. M., & Cohen, J. G. 1996, AJ, 112, 839
Csabai, I., et al. 2003, AJ, 125, 580
Di Matteo, T., Springel, V., & Hernquist, L. 2005, Nature, 433, 604
Dressler, A., Thompson, I. B., & Shectman, S. A. 1985, ApJ, 288, 481
Evans, M., Hastings, N., & Peacock, B. 2000, Statistical Distributions (3rd ed.; New York: Wiley-Interscience)
Fabbiano, G. 2006, ARA&A, 44, 323
Faber, S. M., et al. 2007, ApJ, 665, 265
Feigelson, E. D., Broos, P., Gaffney, III, J. A., Garmire, G., Hillenbrand, L. A., Pravdo, S. H., Townsley, L., & Tsuboi, Y. 2002, ApJ, 574, 258
Ferrarese, L., & Merritt, D. 2000, ApJ, 539, L9
Freeman, P. E., Kashyap, V., Rosner, R., & Lamb, D. Q. 2002, ApJS, 138, 185
Fukugita, M., Ichikawa, T., Gunn, J. E., Doi, M., Shimasaku, K., & Schneider, D. P. 1996, AJ, 111, 1748
Gebhardt, K., et al. 2000, ApJ, 539, L13
Gehrels, N. 1986, ApJ, 303, 336
Georgakakis, A., Gerke, B. F., Nandra, K., Laird, E. S., Coil, A. L., Cooper, M. C., & Newman, J. A. 2008a, MNRAS, 391, 183
Georgakakis, A., et al. 2008b, MNRAS, 385, 2049
Georgantopoulos, I., & Georgakakis, A. 2005, MNRAS, 358, 131
Giovanelli, R., & Haynes, M. P. 1985, ApJ, 292, 404
Granato, G. L., De Zotti, G., Silva, L., Bressan, A., & Danese, L. 2004, ApJ, 600, 580
Green, P. J., et al. 2004, ApJS, 150, 43
Green, P. J., et al. 2009, ApJ, 690, 644
Gültekin, K., et al. 2009, ApJ, 698, 198
Hasinger, G., Miyaji, T., & Schmidt, M. 2005, A&A, 441, 417
Heckman, T. M., Ptak, A., Hornschemeier, A., & Kauffmann, G. 2005, ApJ, 634, 161
Hernquist, L. 1989, Nature, 340, 687
Ho, L. C. 2008, ARA&A, 46, 475
Hogg, D. W., et al. 2002, AJ, 124, 646
Hopkins, P. F., Hernquist, L., Cox, T. J., & Kereš, D. 2008, ApJS, 175, 356
Hopkins, P. F., Hernquist, L., Martini, P., Cox, T. J., Robertson, B., Di Matteo, T., & Springel, V. 2005, ApJ, 625, L71
Hopkins, P. F., Somerville, R. S., Hernquist, L., Cox, T. J., Robertson, B., & Li, Y. 2006, ApJ, 652, 864
Hornschemeier, A. E., Heckman, T. M., Ptak, A. F., Tremonti, C. A., & Colbert, E. J. M. 2005, AJ, 129, 86
Hornschemeier, A. E., et al. 2000, ApJ, 541, 49
Kauffmann, G., White, S. D. M., Heckman, T. M., Ménard, B., Brinchmann, J., Charlot, S., Tremonti, C., & Brinkmann, J. 2004, MNRAS, 353, 713
Kauffmann, G., et al. 2003, MNRAS, 346, 1055
Kewley, L. J., Dopita, M. A., Sutherland, R. S., Heisler, C. A., & Trevena, J. 2001, ApJ, 556, 121
Kim, M., Wilkes, B. J., Kim, D., Green, P. J., Barkhouse, W. A., Lee, M. G., Silverman, J. D., & Tananbaum, H. D. 2007a, ApJ, 659, 29
Kim, D., et al. 2006, ApJ, 644, 829
Kim, M., et al. 2007b, ApJS, 169, 401
Kurtz, M. J., & Mink, D. J. 1998, PASP, 110, 934
Lehmer, B. D., et al. 2007, ApJ, 657, 681
Lehmer, B. D., et al. 2008, ApJ, 681, 1163
Lilly, S. J., Tresse, L., Hammer, F., Crampton, D., & Le Fevre, O. 1995, ApJ, 455, 108
Lupton, R. H., Ivezic, Z., Gunn, J. E., Knapp, G., Strauss, M. A., & Yasuda, N. 2002, Proc. SPIE, 4836, 350
Marconi, A., Risaliti, G., Gilli, R., Hunt, L. K., Maiolino, R., & Salvati, M. 2004, MNRAS, 351, 169
Martini, P. 2004, in IAU Symp. 222, The Interplay Among Black Holes, Stars and ISM in Galactic Nuclei, ed. T. Storchi-Bergmann, L. C. Ho, & H. R. Schmitt (Cambridge: Cambridge Univ. Press), 235
Martini, P., Kelson, D. D., Kim, E., Mulchaey, J. S., & Athey, A. A. 2006, ApJ, 644, 116
Martini, P., Kelson, D. D., Mulchaey, J. S., & Trager, S. C. 2002, ApJ, 576, L109
Martini, P., Mulchaey, J. S., & Kelson, D. D. 2007, ApJ, 664, 761
Martini, P., Sivakoff, G. R., & Mulchaey, J. S. 2009, ApJ, 701, 66
Miller, C. J., Nichol, R. C., Gómez, P. L., Hopkins, A. M., & Bernardi, M. 2003, ApJ, 597, 142
Munn, J. A., et al. 2004, AJ, 127, 3034
Munn, J. A., et al. 2008, AJ, 136, 895
Myers, A. D., White, M., & Ball, N. M. 2009, MNRAS, 399, 2279
Oyaizu, H., Lima, M., Cunha, C. E., Lin, H., Frieman, J., & Sheldon, E. S. 2008, ApJ, 674, 768
Padmanabhan, N., et al. 2007, MNRAS, 378, 852
Padmanabhan, N., et al. 2008, ApJ, 674, 1217
Page, M. J. 2001, MNRAS, 328, 925
Pier, J. R., Munn, J. A., Hindsley, R. B., Hennessy, G. S., Kent, S. M., Lupton, R. H., & Ivezić, Ž. 2003, AJ, 125, 1559
Popesso, P., & Biviano, A. 2006, A&A, 460, L23
Prieto, M. A., Reunanen, J., Tristram, K. R. W., Neumayer, N., Fernandez-Ontiveros, J. A., Orienti, M., & Meisenheimer, K. 2010, MNRAS, 402, 724
Rees, M. J. 1984, ARA&A, 22, 471
Richards, G. T., et al. 2001, AJ, 122, 1151
Richards, G. T., et al. 2002, AJ, 123, 2945
Richards, G. T., et al. 2009, ApJS, 180, 67
Scannapieco, E., Silk, J., & Bouwens, R. 2005, ApJ, 635, L13
Schawinski, K., et al. 2010, ApJ, 711, 284
Scranton, R., et al. 2002, ApJ, 579, 48
Shankar, F., Salucci, P., Granato, G. L., De Zotti, G., & Danese, L. 2004, MNRAS, 354, 1020
Shi, Y., Rieke, G., Donley, J., Cooper, M., Willmer, C., & Kirby, E. 2008, ApJ, 688, 794
Silverman, J. D., et al. 2008, ApJ, 675, 1025
Silverman, J. D., et al. 2009a, ApJ, 695, 171
Silverman, J. D., et al. 2009b, ApJ, 696, 396
Soltan, A. 1982, MNRAS, 200, 115
Stoughton, C., et al. 2002, AJ, 123, 485
Strateva, I., et al. 2001, AJ, 122, 1861
Sun, M., Jones, C., Forman, W., Vikhlinin, A., Donahue, M., & Voit, M. 2007, ApJ, 657, 197
Ueda, Y., Akiyama, M., Ohta, K., & Miyaji, T. 2003, ApJ, 598, 886
Weinstein, M. A., et al. 2004, ApJS, 155, 243
Weisskopf, M. C., Brinkman, B., Canizares, C., Garmire, G., Murray, S., & Van Speybroeck, L. P. 2002, PASP, 114, 1
Wolf, C., Meisenheimer, K., Rix, H., Borch, A., Dye, S., & Kleinheinrich, M. 2003, A&A, 401, 73
Wright, E. L. 2006, PASP, 118, 1711
Yan, R., & Ho, L. AEGIS Collaboration 2010, BAAS, 41, 419
York, D. G., et al. 2000, AJ, 120, 1579
Yu, Q., & Tremaine, S. 2002, MNRAS, 335, 965
Zezas, A. L., Georgantopoulos, I., & Ward, M. J. 1998, MNRAS, 301, 915